

# Flow Matching at Scale: A Machine Learning Framework for Efficient Large-Size Sampling of Many-Body Systems

Qian-Rui Lee<sup>1</sup> and Daw-Wei Wang<sup>1,2,3</sup>

<sup>1</sup>*Physics Department, National Tsing Hua University, Hsinchu 30013, Taiwan*

<sup>2</sup>*Center for Theory and Computation, National Tsing Hua University, Hsinchu 30013, Taiwan*

<sup>3</sup>*Center for Quantum Technology, National Tsing Hua University, Hsinchu 30013, Taiwan*

(Dated: August 22, 2025)

We propose a machine learning framework based on Flow Matching to overcome the scaling limitations of Markov Chain Monte Carlo (MCMC) methods. We demonstrate its capability in the 2D XY model, where a single network, trained only on configurations from a small ( $32 \times 32$ ) lattice at sparse temperature points, generates reliable samples for a significantly larger system ( $128 \times 128$ ) across a continuous temperature range without retraining. The generated configurations show strong agreement with key thermodynamic observables and correctly capture the signatures of the Berezinskii-Kosterlitz-Thouless (BKT) transition. This dual generalization is enabled by the Flow Matching framework, which allows us to learn a continuous, temperature-conditioned mapping. At the same time, the inductive biases of the underlying CNN architecture ensure that the learned local physical rules are scale-invariant. This "train-small, generate-large" capability establishes a new paradigm for efficiently studying critical phenomena, offering a significant computational advantage for exploring the thermodynamic limit. The method can be directly applied to other classical or quantum many-body systems described by continuous fields on a lattice.

## I. INTRODUCTION

Monte Carlo—especially Markov chain Monte Carlo (MCMC)—is one of the most powerful computational tools across three fronts: in condensed matter, it is the workhorse for probing phase transitions and complex systems [1]; in quantum many-body physics, quantum Monte Carlo is among the few reliable non-perturbative methods [2, 3]; and in lattice QCD, Euclidean-lattice Monte Carlo provides the only systematically improvable first-principles non-perturbative approach at low energies [4, 5]. Algorithmically, MCMC targets the Boltzmann measure via detailed balance and ergodicity (e.g. Metropolis, HMC [6], cluster [7]), with uncertainties governed by the integrated autocorrelation time [1].

However, MCMC encounters critical slowing down as correlation lengths grow near continuous phase transitions and toward the continuum limit; in lattice QCD, topological modes can freeze, inflating autocorrelations and complicating error estimates [8]. Fermionic models further face the sign problem, whose generic resolution is NP-hard [9]. Progress relies on advanced updates [7], tempering/multilevel schemes [10], and ML-assisted samplers; notably, flow-based generative sampling have shown decorrelated proposals and efficiency gains in lattice field theories [11].

Early successes with models like Normalizing Flows (NFs) demonstrated the potential to eliminate critical slowing down for a single set of system parameters [11, 12]. However, the inefficiency of these initial approaches in exploring parameter space is a significant limitation. Studying critical phenomena requires simulations across various parameters (e.g., temperatures), but training a separate, computationally expensive model for each point is impractical [13]. A key advancement to address this has been the development of conditional mod-

els, which learn the system's behavior across a continuous parameter range from sparse training data, enabling efficient interpolation and extrapolation [13, 14]. These models are often implemented with either architecturally rigid NFs, which can suffer from training instabilities like mode collapse [12, 15], or with Diffusion Models (DM), which, while robust, typically rely on a computationally intensive iterative sampling process [16, 17].

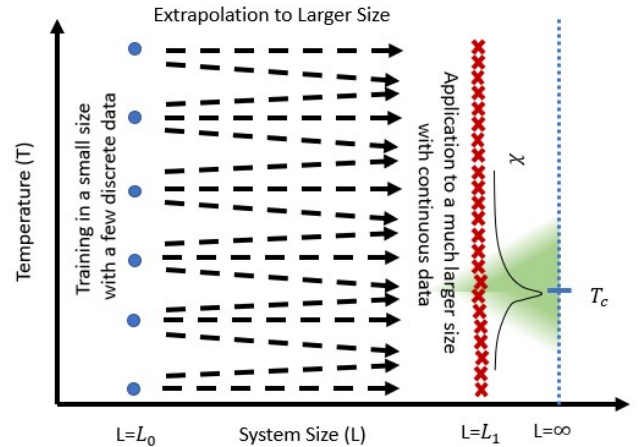


FIG. 1. Schematic diagram of our work. Using Flow Matching with U-Net [18] inductive biases, we learn a deterministic probability-flow sampler that—trained only on  $L_0 \times L_0$  lattices—simultaneously interpolates across temperatures and extrapolates (dashed lines) to physically consistent configurations of  $L_1 \times L_1$  lattices with  $L_1 \gg L_0$ , revealing scale-invariant rules and enabling a fast and stable exploration of critical phenomena near the critical temperature,  $T_c$ . Here  $\chi$  denotes the susceptibility, and the green shadow represents the critical regime.

Even as conditional models begin to address the challenge of exploring parameter space, a more fundamental and computationally demanding limitation persists in both traditional MCMC and these new generative approaches: the lack of generalizability across system sizes. Systematic studies of critical phenomena and the thermodynamic limit hinge on a sequence of simulations on progressively larger lattices. Under the current paradigm, each lattice size requires an entirely new, independent simulation or model training, a process whose computational cost scales prohibitively. Therefore, a truly efficient framework would not only interpolate across parameters like temperature but also learn the underlying, scale-invariant physical rules, enabling extrapolation from a single, small-system training process to much larger lattices. Our work is designed to address this critical gap directly.

In this work, we employ Flow Matching (FM) [19], a next-generation framework that combines the advantages of these preceding approaches while mitigating their drawbacks. FM directly learns the deterministic vector field of a continuous transformation, known as the probability flow ODE [20]. This provides a more stable regression-based training objective than traditional NFs and enables significantly faster sampling than the stochastic processes of DMs [20, 21]. This training stability, architectural flexibility, and sampling efficiency combination makes FM an ideal candidate for building a robust and generalizable conditional sampler. When integrated with the strong inductive biases of a U-Net architecture [18], we demonstrate that this superior framework solves a crucial remaining challenge: achieving a robust dual generalization. We show that a single model, trained only on data from a small lattice ( $32 \times 32$ ), can simultaneously interpolate across a continuous temperature range and extrapolate to generate physically consistent configurations for substantially larger systems (up to  $128 \times 128$ ). This capability to learn scale-invariant physical rules from limited data establishes our approach as a computationally superior paradigm for efficiently investigating critical phenomena in the thermodynamic limit.

The paper is organized as follows. We begin by introducing the theoretical framework of Flow Matching in Sec. II and our simulation setup in Sec. III. Our main numerical results and analyses, covering the model’s dual generalization, performance, and efficiency, are presented in Secs. IV to VII. We then provide a physical interpretation for these capabilities in Sec. VIII. The paper concludes with a discussion of our findings in Sec. IX and an outlook for future work in Sec. X.

## II. THEORETICAL STRUCTURE OF FLOW MATCHING

Flow Matching bridges continuous NFs and diffusion models by directly learning vector fields (flows) along pre-defined conditional probability paths between a simple

base distribution (e.g., Gaussian noise) and the target data distribution. It trains models by regressing on these conditional velocities rather than relying on stochastic simulations, resulting in stable, scalable training and efficient sample generation via off-the-shelf ODE solvers.

### A. Probability Flow ODE

Flow Matching admits arbitrary paths, granting flexibility to optimize sampling speed or modeling capacity [19]. In this work, we adopt a simple linear interpolation between base and data for simplicity. For a target data sample  $\mathbf{x}_1 \sim \mathcal{P}_{data}$  and a standard Gaussian noise sample  $\mathbf{x}_0 \sim \mathcal{N}(0, \mathbb{I})$  of the same dimensionality, we define the path  $\{\mathbf{x}_t\}_{t=0}^1$ , where  $t$  is a virtual time parameter indexing the continuous evolution of the distribution. The path at each subscripted time  $t$  is given by

$$\mathbf{x}_t = t \mathbf{x}_1 + (1 - t) \mathbf{x}_0 \quad (1)$$

For a fixed coupling  $(\mathbf{x}_0, \mathbf{x}_1)$ , the conditional velocity field is

$$\mathbf{v}_t(\mathbf{x}_t|\mathbf{x}_1) = \frac{d\mathbf{x}_t}{dt} = \mathbf{x}_1 - \mathbf{x}_0 \quad (2)$$

But since  $(\mathbf{x}_0, \mathbf{x}_1)$  are random,  $\mathbf{v}_t(\mathbf{x}_t|\mathbf{x}_1)$  is also random. The true velocity field  $\mathbf{u}_t(x)$  is an average of multiple conditional velocity fields. To know this average, consider a distribution  $p_t(x)$  which satisfies the following boundary conditions.

$$p_{t=1}(\mathbf{x}_{t=1}) = \mathcal{P}_{data} \quad \text{and} \quad p_{t=0}(\mathbf{x}_{t=0}) = \mathcal{N}(0, \mathbb{I}). \quad (3)$$

For simplicity, we can denote the configuration of all conditions as the variable  $\phi$ , which satisfies the distribution  $q(\phi)$ . The distribution of the probability path  $p_t(\mathbf{x}_t)$  can be written as

$$p_t(\mathbf{x}_t) = \int [\mathcal{D}\phi] p_t(\mathbf{x}_t|\phi) q(\phi) \quad (4)$$

Here,  $p_t(\mathbf{x}_t|\phi)$  is the conditional probability path. For example, suppose that  $\mathcal{P}_{data}$  is the Boltzmann distribution  $\exp(-\beta H)/Z$ . The configuration  $\phi$  of conditions is only the spin configurations  $\mathbf{x}_1$  (generally, the condition can include temperatures, coupling constants, and other information that may affect the target distribution). Consider the path  $\mathbf{x}_t$  in Eq. (1), because we choose  $\mathbf{x}_0$  that satisfies the standard Gaussian distribution, therefore, conditional probability  $p_t(\mathbf{x}_t|\mathbf{x}_1)$  is the Gaussian distribution with mean  $t\mathbf{x}_1$  and variance  $(1-t)^2 \mathbb{I}$  [22]. The  $p_t(\mathbf{x}_t)$  hence reads as

$$p_t(\mathbf{x}_t) = \int [\mathcal{D}\mathbf{x}_1] \mathcal{N}(\mathbf{x}_t; t\mathbf{x}_1, (1-t)^2 \mathbb{I}) \frac{e^{-\beta H(\mathbf{x}_1)}}{Z} \quad (5)$$

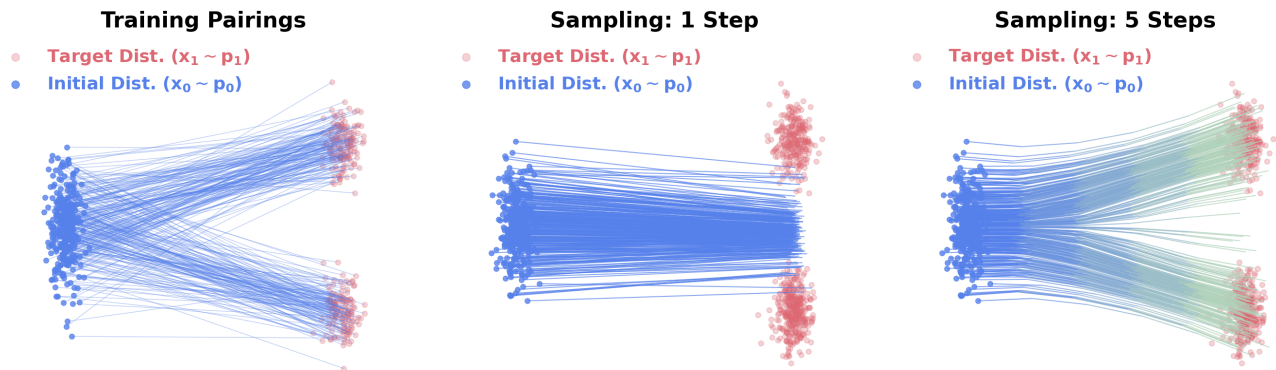


FIG. 2. A naive Flow Matching example. When Flow Matching is trained as a deterministic ODE, trajectories from  $\mathbf{v}_\theta$  deviate from the straight interpolation in Eq. (1). This is because  $\mathbf{v}_\theta$  learns the expectation of the conditional velocity,  $\mathbf{v}_t(\mathbf{x}_t|\phi)$ , induced by the random pairings of  $(\mathbf{x}_0, \mathbf{x}_1)$  during training (left panel). Consequently, the first sampling step (middle panel) points toward the target mean; with a finite number of iterations, inference preferentially produces samples near this mean, thereby underrepresenting the target variance and fluctuations.

We can easily check that Eq. (5) satisfies the requirements in Eq. (3).

With conditional velocity field  $\mathbf{v}_t(\mathbf{x}_t|\phi)$  and probability density  $p_t(\mathbf{x}_t)$  in Eq. (4), the continuity equation gives

$$\frac{\partial p_t(\mathbf{x}_t)}{\partial t} = -\nabla \cdot \int [\mathcal{D}\phi] \mathbf{v}_t(\mathbf{x}_t|\phi) p_t(\mathbf{x}_t|\phi) q(\phi) \quad (6)$$

Thus, with Bayes' theorem, the velocity field  $\mathbf{u}_t(\mathbf{x}_t)$  is

$$\begin{aligned} \mathbf{u}_t(\mathbf{x}_t) &= \int [\mathcal{D}\phi] \mathbf{v}_t(\mathbf{x}_t|\phi) \frac{p_t(\mathbf{x}_t|\phi) q(\phi)}{p_t(\mathbf{x}_t)} \\ &= \int [\mathcal{D}\phi] \mathbf{v}_t(\mathbf{x}_t|\phi) p_t(\phi|\mathbf{x}_t) \end{aligned} \quad (7)$$

The corresponding ODE to  $\mathbf{u}_t(\mathbf{x}_t)$  is also called the probability flow ODE [20]:

$$\frac{d\mathbf{x}_t}{dt} = \mathbf{u}_t(\mathbf{x}_t) \quad (8)$$

And we want the neural network  $\mathbf{v}_\theta$  with learnable parameters  $\theta$  to learn this velocity field  $\mathbf{u}_t(\mathbf{x}_t)$ .

## B. Loss Function

With the probability flow ODE in Eq (8), the Flow Matching loss  $\mathcal{L}_{FM}(\theta)$  can be defined as

$$\mathcal{L}_{FM}(\theta) \equiv \int_0^1 dt \int [\mathcal{D}\mathbf{x}_t] p_t(\mathbf{x}_t) [\mathbf{v}_\theta(\mathbf{x}_t, t) - \mathbf{u}_t(\mathbf{x}_t)]^2 \quad (9)$$

However, we do not know the exact velocity field  $\mathbf{u}_t(\mathbf{x}_t)$  from the training data. Thus, use the trick that the gradient of the loss function  $\mathcal{L}(\theta)$  to update the neural network  $\mathbf{v}_\theta$  is only depend on  $\theta$ , it is equivalent [19] to define conditional Flow Matching loss  $\mathcal{L}_{CFM}(\theta)$  that we want to minimize as

$$\begin{aligned} \mathcal{L}_{CFM}(\theta) &\equiv \\ &\int_0^1 dt \int [\mathcal{D}\mathbf{x}_0 \mathcal{D}\phi] p_t(\mathbf{x}_t|\phi) q(\phi) [\mathbf{v}_\theta(\mathbf{x}_t, t|\phi) - \mathbf{v}_t(\mathbf{x}_t|\phi)]^2 \end{aligned} \quad (10)$$

The loss function is similar to the action of the noninteracting fluid system with integration in the entire condition configuration  $\phi$  and the initial Gaussian noise. For the path in Eq. (1), conditional velocity field  $\mathbf{v}_t(\mathbf{x}_t|\phi)$  here is just  $(\mathbf{x}_1 - \mathbf{x}_0)$  and see the Appendix A for more details.

## C. Flow of Random Sampling

Although the path in Eq. (1) is straight, but the training paths are created by randomly pairing data  $\mathbf{x}_1$  and noise  $\mathbf{x}_0$  with different conditions. Therefore, different conditional trajectories passing through the same  $x_t$  at time  $t$  generally have different directions, and the velocity field  $\mathbf{u}_t(\mathbf{x}_t)$  is not identical to the constant vector  $(\mathbf{x}_1 - \mathbf{x}_0)$  (see Fig. 2). What the neural network  $\mathbf{v}_\theta(\mathbf{x}_t, t|\phi)$  learned is an expectation over conditional velocities and there is inherent uncertainty about the direction. One way to understand this is to view the training path as a quantum process, where a sample from the initial distribution  $\mathbf{x}_0$  has the opportunity to reach any target distribution  $\mathbf{x}_1$ . Flow matching allows the neural network to learn the generators corresponding to the

path that contributes most, the classical path. Due to this reason, instead of collapsing sampling to a single jump from noise to data, we must integrate the learned velocity field over a few time steps (however, research on the one-step sampling is rapidly expanding [23, 24]). Concretely, we divide the interval  $t \in [0, 1]$  into  $N$  steps  $\{t_k\}_{k=0}^N$  and numerically solve the problem.

$$\frac{d\mathbf{x}_t}{dt} = \mathbf{v}_\theta(\mathbf{x}_t, t|\phi) \quad (11)$$

using a method such as explicit Euler or a higher-order Runge–Kutta. Then, we can transport the samples from the distribution  $p_0$  to  $p_1$ . For more training and sampling details, see the Appendix B.

### III. SIMULATION FRAMEWORK

#### A. Parameter-Wide Sampling via a Single Network

One of the main advantages of flow-based sampling is that it can generate target samples in parallel and independently, thus avoiding the autocorrelation problem of traditional MCMC sampling. This advantage can be easily maximized in the Flow Matching training framework. To construct the conditional velocity field in Eq. (2), only two types of information are required as conditions ( $\phi$ ): one is the samples ( $\mathbf{x}_1$ ) that obey the target distribution, and the other are the parameters (e.g., temperature in this work) corresponding to the samples. The Flow Matching framework can construct probability flows in completely parallel across the above two data dimensions. For example, the target samples  $\mathbf{x}_1$  in this work have two indices: temperature and ensemble. Assuming that we have data corresponding to  $N_T$  temperatures within a range, and each temperature has  $N_{cf}$  spin configurations, the target sample  $\mathbf{x}_1$ , as a data array, has the shape  $(N_T, N_{cf}, L, L)$ , where  $L$  is the length and width of the lattice. Accordingly, the trained network  $\mathbf{v}_\theta(\mathbf{x}_t, t, T)$  can generate, in parallel, arbitrarily large ensembles of independent  $L \times L$  samples across the training temperature range.

#### B. 2D XY Model and Physical Observables

To benchmark our framework, we use the standard two-dimensional (2D) XY model, defined on a square lattice of size  $N = L \times L$ . The system is described by the Hamiltonian:

$$H = - \sum_{\langle i,j \rangle} \cos(\Theta_i - \Theta_j) \quad (12)$$

where  $\Theta_i \in (-\pi, \pi]$  is the angle of the spin at site  $i$ , and the sum runs over all nearest-neighbor pairs.

The canonical average of any thermodynamic observable  $O$  is calculated over an ensemble of configurations:

$$\langle O \rangle = \frac{1}{N_{cf}} \sum_{k=1}^{N_{cf}} O_k \quad (13)$$

where  $O_k$  is the value of the observable for the  $k$ -th configuration and  $N_{cf}$  is the total number of configurations in the ensemble. All intensive quantities are averaged over the  $N$  lattice sites and the ensemble, as defined in Eq. (13). Throughout this work, the temperature  $T$  is expressed in units where the Boltzmann constant  $k_B = 1$ .

The energy per site is derived directly from the Hamiltonian:

$$E \equiv \frac{1}{N} \langle H \rangle \quad (14)$$

The Cartesian components of the total magnetization are:

$$M_x \equiv \sum_{i=1}^N \cos(\Theta_i), \quad M_y \equiv \sum_{i=1}^N \sin(\Theta_i) \quad (15)$$

and the root-mean-square (RMS) magnetization per site is:

$$m \equiv \frac{1}{N} \left\langle \sqrt{M_x^2 + M_y^2} \right\rangle \quad (16)$$

The zero-field susceptibility is given by the fluctuations of the magnetization:

$$\chi \equiv \frac{1}{NT} \left( \langle M_x^2 + M_y^2 \rangle - \left\langle \sqrt{M_x^2 + M_y^2} \right\rangle^2 \right) \quad (17)$$

To define the spin stiffness, we consider the negative Hamiltonian and the spin current restricted to bonds crossing the lattice in the  $y$ -direction:

$$h_y \equiv \sum_{\langle i,j \rangle_y} \cos(\Theta_i - \Theta_j), \quad I_y \equiv \sum_{\langle i,j \rangle_y} \sin(\Theta_i - \Theta_j) \quad (18)$$

The spin stiffness is then defined as [2]:

$$\rho_s \equiv \frac{1}{N} \left( \langle h_y \rangle - \frac{1}{T} \langle I_y^2 \rangle \right) \quad (19)$$

Finally, the vortex density is obtained by summing the absolute winding number over each elementary  $1 \times 1$  plaquette ( $\square$ ):

$$\rho_v \equiv \frac{1}{N} \left\langle \sum_{\square} \left| \frac{1}{2\pi} \sum_{\langle i,j \rangle \in \partial \square} [\Theta_j - \Theta_i]_{2\pi} \right| \right\rangle \quad (20)$$

where the inner sum is over the four bonds forming the plaquette's boundary  $\partial \square$ , and  $[\dots]_{2\pi}$  wraps the angle difference into the interval  $(-\pi, \pi]$ .

The training data, consisting of spin configurations  $\mathbf{x}_1$ , uses angles mapped to the range  $[0, 2\pi)$ . The neural

network is trained to directly output continuous angular values without an explicit modular arithmetic operation (i.e., no wrapping into  $(-\pi, \pi]$  or  $[0, 2\pi)$ ). This is a valid approach because all relevant physical observables, such as the energy and magnetization components, are calculated using trigonometric functions (e.g.,  $\cos(\Theta_i - \Theta_j)$  and  $\sin(\Theta_i)$ ), which are inherently periodic with a period of  $2\pi$ .

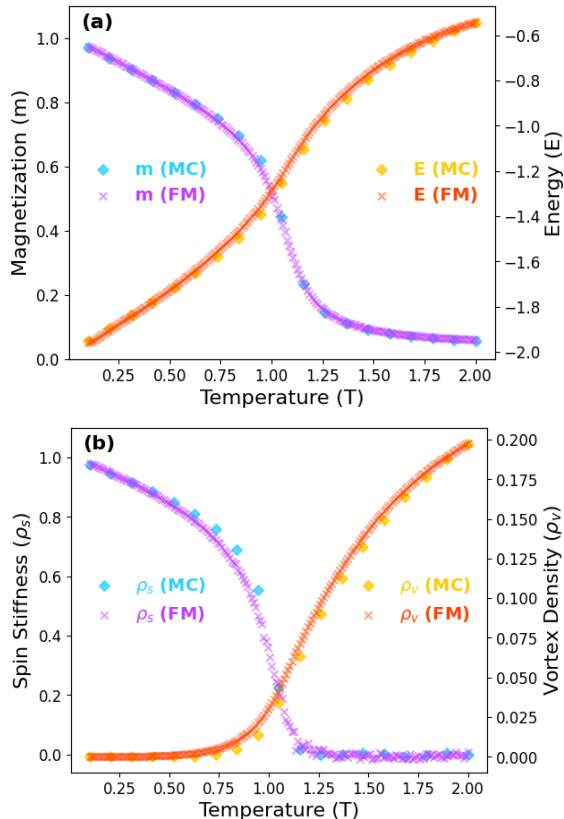


FIG. 3. Thermodynamic observables for the  $32 \times 32$  XY model, demonstrating the Flow Matching (FM) model’s ability to increase sampling density via interpolation. The panels show (a) energy per site  $E(T)$  and magnetization  $m(T)$ , and (b) spin stiffness  $\rho_s(T)$  and vortex density  $\rho_v(T)$ . The sparse points represent MCMC (MC) data, which serves as the training set, sampled at a coarse temperature interval of  $\Delta T = 0.10$ . Each of these points was generated from an ensemble of 5000 configurations. The denser set of points shows the results from FM, evaluated on a tenfold denser grid ( $\Delta T = 0.01$ ), confirming agreement with and smooth interpolation between the training points.

#### IV. RESULT I: ACCURATE INTERPOLATION OF PARAMETER DENSITY

Flow Matching can learn the transfer of the data background distribution through limited data, so the most

intuitive benefit is that one can train the model through discrete samples in parameter space and then make continuous predictions. Just like when one pulls the tablecloth, the petals on the tablecloth will move accordingly. When the tablecloth pulling method is learned and fixed, no matter how many petals are sprinkled, there will be the same movement pattern. Here we show that Flow Matching trained with MC data at intervals of 0.1 in the temperature range of  $0.1 \sim 2.0$  can be easily sampled with ten times the temperature density (intervals of 0.01). Figs. 3 show that the spin configuration sampling results of Flow Matching still retain good physical statistical properties after increasing the temperature density.

Flow Matching provides an additional benefit and advantage in parameter interpolation. Certain physical quantities, such as susceptibility, often exhibit complex and abrupt changes near phase transition points as temperature varies. When data points are sparse along the temperature axis, conventional numerical fitting or machine learning methods typically struggle to perform effective interpolation. However, although these physical observables change abruptly and complexly, the underlying probability distributions of the samples may vary simply and uniformly concerning certain parameters, such as temperature. In the example of the two-dimensional XY model, as long as Flow Matching accurately learns the relationship between the probability distribution of samples and temperature, it can effectively generate samples within temperature ranges where training data are sparse. Fig. 4 shows that Flow Matching, trained on spin configuration samples that are extremely sparse in temperature, can still produce samples that exhibit qualitatively consistent statistical properties.

#### V. RESULT II: RELIABLE EXTRAPOLATION OF SYSTEM SIZES

A key strength of our Flow Matching approach is its ability to extrapolate to different system sizes without retraining. This capability is central to our study’s primary goal: to demonstrate that Flow Matching can efficiently capture the essential underlying physics of a system from limited data, prioritizing qualitative consistency over precise quantitative reproduction. As shown in Fig. 5, a single model trained exclusively on  $32 \times 32$  configurations successfully generates samples for a  $64 \times 64$  system. The results for key observables exhibit strong qualitative agreement with the reference MC data, confirming that the learned physical rules are generalized effectively.

This extrapolation is robust across a wide range of system dimensions. As shown in Figs. 6 and 7, the same model trained on  $32 \times 32$  generates configurations for lattices as small as  $16 \times 16$  and as large as  $128 \times 128$ . Although quantitative deviations increase with the extrapolation range, the model correctly captures essential finite-size effects, such as the characteristic shift and sharpening of the susceptibility peak, a key signature of

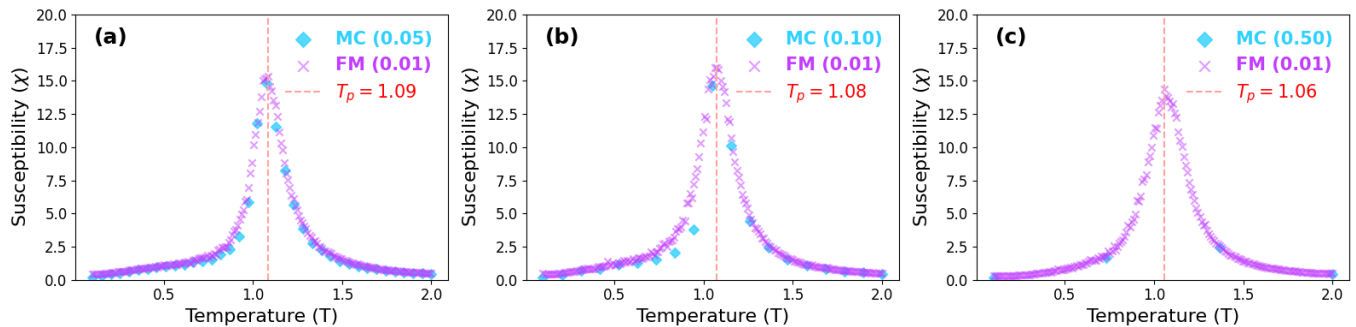


FIG. 4. Susceptibility  $\chi(T)$  for a  $32 \times 32$  XY lattice. The points show results from MCMC (MC) simulations, which serve as both the ground truth and the training data for our Flow Matching (FM) model. The three panels demonstrate the model’s performance when trained on this MCMC data at varying levels of precision: (a) a dense grid with temperature spacing  $\Delta T = 0.05$ , (b)  $\Delta T = 0.10$ , and (c) a sparse grid with  $\Delta T = 0.50$ . The training data consists of 5000 configurations per temperature point. In all cases, the FM model is evaluated on a much finer grid ( $\Delta T = 0.01$ ), showing it successfully reproduces the BKT-related features even when trained on the sparsest data set.

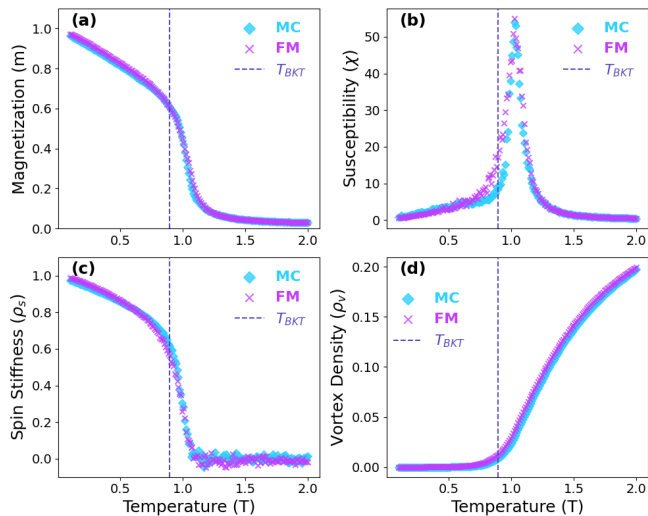


FIG. 5. Size extrapolation results for the Flow Matching (FM) model. The model was trained on data from a  $32 \times 32$  system ( $T \in [0.1, 2.0]$ ,  $\Delta T = 0.01$ , 1500 configs/T) and then used to generate configurations for a  $64 \times 64$  lattice. The generated observables—(a) magnetization, (b) susceptibility, (c) spin stiffness, and (d) vortex density—are shown to be in good agreement with reference MCMC results for the larger system.

the BKT transition. This preservation of qualitative features underscores the model’s ability to learn fundamental physical behavior.

A finite-size scaling analysis tests the model’s ability to learn scale-invariant physics. Our primary objective here is to qualitatively demonstrate this emergent capability, rather than to achieve a high-precision estimate of  $T_{BKT}$ . We acknowledge that spin stiffness is a more rigorous metric for analyzing the BKT transition [25]. However, as discussed in our error analysis (Sec. VI), the model’s predictions for fluctuation-related quantities are inherently less precise, a characteristic compounded

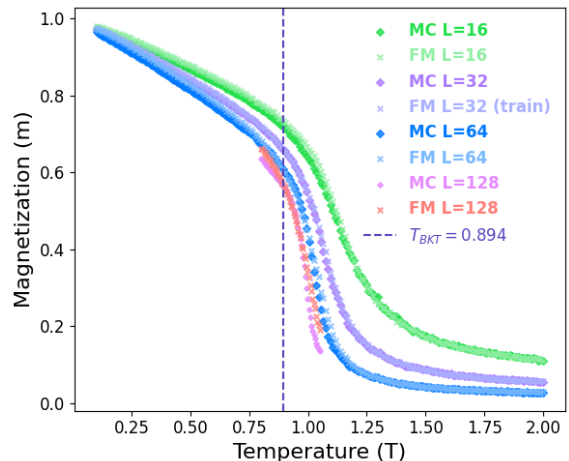


FIG. 6. Size extrapolation of magnetization using a single Flow Matching (FM) model trained only on a  $32 \times 32$  lattice ( $T \in [0.1, 2.0]$ ,  $\Delta T = 0.01$ , 1500 configs/T). The model generates configurations for various system sizes ( $L = 16, 64, 128$ ), and the resulting magnetization is compared against MCMC (MC) data. The FM results match the reference data for each individual size and correctly exhibit the characteristic finite-size scaling trend of the transition.

by our deliberate use of a limited, low-precision training dataset (1500 configurations per temperature from MCMC). Consequently, the statistical noise in the generated stiffness data, particularly near the critical point, was too significant to permit a reliable scaling analysis. We transparently document this behavior alongside other observables in Appendix C.

In contrast, the location of the susceptibility peak,  $T_{\text{peak}}(L)$ , provided a more robust and clearly identifiable feature for demonstrating the expected scaling behavior. We therefore adopted this metric for our analysis. Using the single model trained on  $32 \times 32$  data, we located  $T_{\text{peak}}(L)$  for various lattice sizes ( $L = 16$  to  $128$ ). As

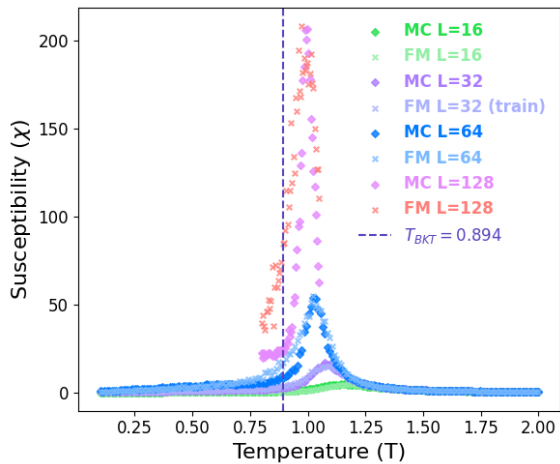


FIG. 7. Susceptibility  $\chi(T)$  for various system sizes ( $L = 16, 64, 128$ ), demonstrating the size-extrapolation capability of a single Flow Matching (FM) model. The model was trained exclusively on  $32 \times 32$  data ( $T \in [0.1, 2.0]$ ,  $\Delta T = 0.01$ , 1500 configs/T). Although quantitative deviations from the MCMC (MC) reference increase as the system size diverges from the training size, the FM model qualitatively captures the essential physics. Specifically, it correctly reproduces the characteristic shift and sharpening of the susceptibility peak with system size, a key signature of the BKT transition.

depicted in Fig. 8, a plot of  $T_{\text{peak}}(L)$  versus  $(\ln L)^{-2}$  reveals the expected linear relationship [26]. Extrapolating to the thermodynamic limit ( $L \rightarrow \infty$ ) yields an estimated  $T_{\text{BKT}} \approx 0.898$ , in reasonable agreement with the established value of  $\approx 0.8935$  [25]. This result, achieved without high-precision training data or retraining, confirms that the model has successfully learned the size-independent physical principles of the XY model, highlighting its efficiency for studying critical phenomena.

## VI. RESULT III: ERRORS ANALYSIS

To quantitatively assess the performance of our Flow Matching model, we compute the mean squared error (MSE) between its predictions and the ground-truth MCMC data for key physical observables, as defined in Eq. (21), where  $T$  is temperature and  $N_T$  is the number of temperature points. Fig. 9 presents this error analysis for a model trained on  $32 \times 32$  lattices and then used to generate samples for systems of size  $L = 16, 32, 64$ , and  $128$ .

$$MSE \equiv \frac{1}{N_T} \sum_T [(\langle \mathcal{O}_{FM}(T) \rangle) - \langle \mathcal{O}_{MC}(T) \rangle]^2 \quad (21)$$

The analysis reveals two important trends. First, the errors for most of quantities are remarkably small, underscoring the high fidelity of the generated samples even when extrapolating to system sizes four times larger than

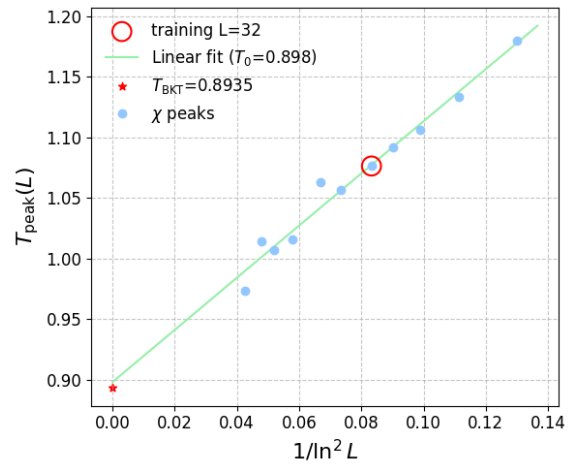


FIG. 8. Finite-size scaling of the BKT transition. The susceptibility peak temperature  $T_{\text{peak}}(L)$  is plotted against  $(\ln L)^{-2}$  for various lattice sizes ( $L = 16, 20, 24, 28, 32, 40, 48, 64, 80, 96, 128$ ). All data points were generated from a single Flow Matching model trained exclusively on  $32 \times 32$  data ( $T \in [0.1, 2.0]$ ,  $\Delta T = 0.01$ , 1500 configs/T). The linear trend, when extrapolated to the thermodynamic limit ( $L \rightarrow \infty$ ), yields  $T_{\text{BKT}} \approx 0.898$ , in good agreement with the established value of  $\approx 0.8935$  [25]. This result confirms that the model has successfully captured the underlying scale-invariant physics.

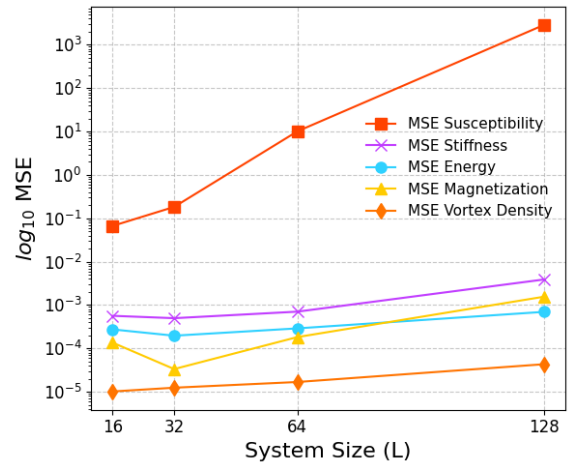


FIG. 9. Mean squared error (MSE) as a function of temperature, quantifying the error of the size extrapolation method. The MSE is calculated between the Flow Matching and reference MCMC results for several observables: susceptibility  $\chi$ , spin stiffness  $\rho_s$ , energy  $E$ , magnetization  $m$ , and vortex density  $\rho_v$ . A single FM model, trained on a  $32 \times 32$  lattice ( $T \in [0.1, 2.0]$ ,  $\Delta T = 0.01$ ), was used to generate data for systems of size  $L = 16, 32, 64$ , and  $128$ . The evaluation for  $L = 16, 32$  and  $64$  uses the same temperature grid as the training, while the evaluation for the largest system,  $L = 128$ , is performed on a finer grid focused on the critical region ( $T \in [0.8, 1.05]$ ,  $\Delta T = 0.005$ ).

the training data. The errors are small for the  $L = 16$  sys-

tem, demonstrating robust interpolation to smaller sizes, and predictably increase with the extrapolation range to  $L = 64$  and  $L = 128$ . Second, and more revealingly, the model exhibits higher accuracy for first-moment quantities like energy ( $E$ ) and magnetization ( $M$ ) compared to second-moment quantities related to fluctuations, such as susceptibility ( $\chi$ ) and spin stiffness ( $\rho_s$ ). This discrepancy is most pronounced near the critical temperature (see Fig. 7), where physical fluctuations are maximal.

This behavior stems from several factors inherent to the Flow Matching framework. Primarily, as discussed in Sec. II C, the model learns to approximate the mean of the conditional velocity field,  $\mathbf{u}_t(\mathbf{x}_t) = \mathbb{E}[\mathbf{v}_t(\mathbf{x}_t|\phi)]$ . This averaging process inherently smooths the learned flow. And it is a direct consequence of the bias-variance trade-off introduced by the mean squared loss function used for training. According to the loss function in Eq. (10), the expected error of the learned velocity field  $\mathbf{v}_\theta$  can be decomposed as:

$$\mathbb{E}[(\mathbf{v}_\theta - \mathbf{v}_t)^2] = (\mathbb{E}[\mathbf{v}_\theta - \mathbf{v}_t])^2 + \text{Var}[\mathbf{v}_\theta - \mathbf{v}_t] \quad (22)$$

To minimize this total error, the model must balance its variance (due to finite training data) against a systematic bias towards the mean of the true conditional velocity field. This optimization naturally produces a learned vector field that under-represents the actual variance of the physical process. Furthermore, this initial inaccuracy in the learned field's variance is compounded during the inference stage. Sampling requires numerical integration of the probability flow ODE with a finite number of steps. As suggested in Fig. 2, the vector guiding the trajectory in each discrete step of the numerical solver is an approximation. Minor errors in the velocity field, particularly regarding its variance, accumulate during the iterative integration process. This can cause the final generated configurations to incorrectly capture the actual spread of the target distribution, leading to a larger error in the variance of the resulting ensemble. Consequently, while the generated samples accurately reflect first-moment quantities such as energy and magnetization, the fluctuation-related properties of the generated ensemble are less reliable. Despite FM-generated samples showing larger errors in fluctuation-related physical statistics, which grow more significantly with size extrapolation, the model remains qualitatively accurate enough to capture essential physics, such as the characteristic peaks in susceptibility, making it a useful tool for identifying phase transitions and performing finite-size scaling analysis.

In the training size ( $32 \times 32$ ), we also analyze the distribution error of the energy versus the different temperature. We use Jensen–Shannon divergence (JSD) as a measure of the difference between Flow Matching and MCMC sampling distributions. For two discrete probability distributions  $\mathcal{P}$  and  $\mathcal{Q}$  in the same domain  $\mathcal{X}$  define the midpoint distribution.

$$\mathcal{M} \equiv \frac{1}{2}(\mathcal{P} + \mathcal{Q}). \quad (23)$$

The Jensen–Shannon divergence (JSD) is given by

$$\text{JSD}(\mathcal{P}||\mathcal{Q}) \equiv \frac{1}{2} \sum_{x \in \mathcal{X}} \mathcal{P}(x) \log \frac{\mathcal{P}(x)}{\mathcal{M}(x)} + \frac{1}{2} \sum_{x \in \mathcal{X}} \mathcal{Q}(x) \log \frac{\mathcal{Q}(x)}{\mathcal{M}(x)}. \quad (24)$$

With natural logarithms,  $0 \leq \text{JSD}(\mathcal{P}||\mathcal{Q}) \leq \ln 2$ , the upper bound  $\ln 2$  is reached precisely when  $\mathcal{P}$  and  $\mathcal{Q}$  are completely unrelated. Fig. 10 shows the JSD of energy distribution at different temperatures. Across most of the temperature range, including the phase transition point ( $T \approx 1.0$  for system size  $32 \times 32$ ), the JSD is less than 0.1, indicating that the Flow Matching sampling results agree with the Monte Carlo simulation. Only near zero temperature does the JSD exceed 0.1. The histograms embedded in Fig. 10 show that the energy distribution becomes increasingly concentrated as the temperature decreases (the bar widths in all histograms are the same). Because Flow Matching uses a neural network model that is simultaneously trained and sampled over the entire temperature range, the figure reveals that under the same conditions, Flow Matching performs relatively poorly for extremely narrow, concentrated distributions.

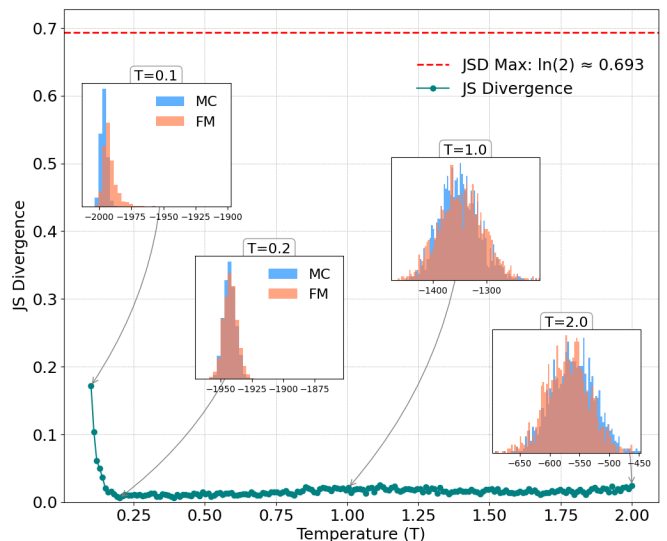


FIG. 10. Jensen–Shannon Divergence (JSD) between the energy distributions generated by the Flow Matching (FM) and MCMC methods as a function of temperature. The analysis was performed on a  $32 \times 32$  lattice, using an FM model trained and evaluated under the specified conditions ( $T \in [0.1, 2.0]$ ,  $\Delta T = 0.01$ , 1500 configs/T). The insets show the corresponding energy histograms at four representative temperatures. All histograms are plotted with identical bin widths to compare the distributions' spread visually. The JSD is highest at very low temperatures, which, as illustrated in the  $T=0.1$  inset, corresponds to a highly concentrated energy distribution that is more challenging for the model to reproduce precisely.

## VII. RESULT IV: COMPUTATIONAL EFFICIENCY FOR LARGE-SCALE STUDIES

The primary computational advantage of our Flow Matching approach stems from its ability to generalize across system sizes, a capability traditional MCMC methods lack. We compare the total time cost required for a typical finite-size scaling analysis to quantify the practical implications of this paradigm shift in workflow. For our FM model, this involves a one-time training cost on a small lattice ( $32 \times 32$ ), followed by rapid inference on a series of larger lattices. The MCMC method requires running a separate, full simulation for each lattice size. We use our highly optimized, GPU-accelerated MCMC algorithm (see Appendix F) as the baseline for this comparison. All timing benchmarks were performed on a single workstation; detailed hardware and software specifications are provided in Appendix G. The key metric for this evaluation is the Sampling Cost, defined as the average wall-clock time to generate a single statistically independent sample:

$$\text{Sampling Cost} \equiv \frac{t_{\text{sample}}}{N_{\text{sample}}} \quad (25)$$

where  $t_{\text{sample}}$  is the total time required to generate  $N_{\text{sample}}$  independent samples across all temperatures and ensembles.

For the FM model, the overall cost has two components: the inference cost, given by Eq. (25), and a one-time, upfront training cost. The average time per configuration during the training phase is defined as:

$$\text{Training Cost} \equiv \frac{t_{\text{train}}}{N_{\text{train}}} \quad (26)$$

where  $t_{\text{train}}$  is the total time to process  $N_{\text{train}}$  training configurations. The training cost here is the amortized time over the total training samples.

As shown in Fig. 11, while the initial training constitutes a significant upfront investment, this cost is amortized over all subsequent sample generation for various larger system sizes. The crossover point at  $L = 128$  demonstrates that our method offers a substantial net reduction in computational resources for comprehensive studies of critical phenomena approaching the thermodynamic limit. This highlights that the actual efficiency of our model lies not in single-sample speed, but in its ability to circumvent the need for repeated, costly simulations across different scales.

## VIII. PHYSICAL INTERPRETATION FOR THE SIZE EXTRAPOLATION

The model’s remarkable ability to generalize across system sizes stems from a carefully engineered synergy between the learning framework, the model architecture, and the fundamental nature of the physical system.

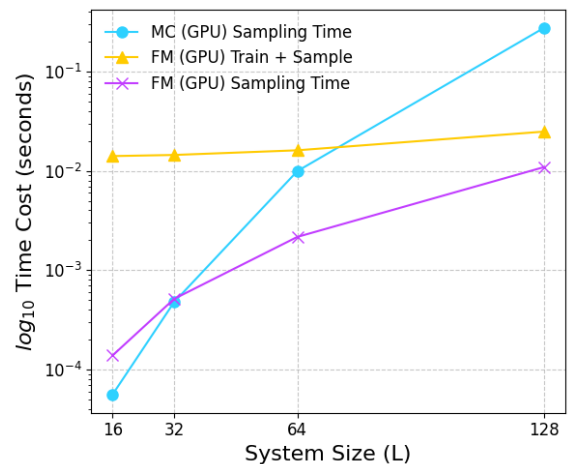


FIG. 11. Computational cost per statistically independent sample as a function of system size  $L$ . The figure compares the performance of our GPU-accelerated MCMC method against the Flow Matching (FM) model, which was trained only on the  $L = 32$  system. The FM cost is presented in two ways: the inference cost alone and the total cost including the amortized one-time training expense, as defined in Eq. (26). The results show a crossover in efficiency, with the FM approach becoming significantly faster than MCMC for large system sizes, establishing its advantage for large-scale studies.

Unlike methods that learn size-specific global statistics, our approach is designed to distill the underlying, scale-invariant local rules dictated by the Hamiltonian. The following subsections will elaborate on the key components that enable this capability. We will first discuss how the strong inductive biases of Convolutional Neural Networks (CNNs), namely locality and translation equivariance, are naturally aligned with the structure of local physical interactions. We will then explain how the specific U-Net architecture leverages these biases across multiple scales to capture both local details and emergent long-range correlations. Finally, we will synthesize these points to argue that the model learns a representation of the local physics itself, which is inherently size-agnostic and thus powerfully generalizable.

### A. Inductive Bias

Inductive bias refers to implicit assumptions within machine learning algorithms that enable generalization to unseen data. The effectiveness of an algorithm depends significantly on how well its inductive biases align with the characteristics of the given task. Thus, selecting an appropriate model involves matching these biases to the specific nature of the problem. For example, several recent studies similar to this work have pointed out that the equivariance of neural networks (a kind of inductive bias) has significant advantages in dealing with physical systems with symmetries [27, 28].

Convolutional Neural Networks (CNNs) inherently contain strong inductive biases that are advantageous for processing natural images whose statistical properties align closely with these biases. Consequently, CNNs efficiently learn visual representations with minimal data. These biases are equally effective in physical systems characterized by local interactions. The core computational mechanism of CNNs is convolution, typically implemented using small convolutional kernels (e.g.  $3 \times 3$  in this work). This design explicitly encodes the inductive bias of locality, which posits that the most relevant information for interpreting any given part of an image is predominantly contained within its spatial vicinity. Thus, the significance of any pixel largely depends on its neighboring pixels, allowing CNN neurons to focus solely on small, localized receptive fields. This notion parallels the physical treatment of complex many-body systems, where interactions are often defined locally. Physicists commonly represent such systems using local Hamiltonians, and physical fields or spin configurations governed by these Hamiltonians naturally conform to CNN’s locality inductive bias, where the state or behavior at a given location is determined by its neighbors.

A second crucial inductive bias inherent in CNNs is translation equivariance, arising from parameter sharing across convolutional layers. Within each convolutional layer, the same kernel systematically traverses the entire input feature map, ensuring that the features and behaviors learned at any specific location can directly inform the interpretations at all other spatial locations. This bias aligns with the practice in physics of using uniform or similarly structured local Hamiltonians to describe complex many-body systems consistently throughout their spatial domain, rather than employing entirely distinct physical mechanisms or Hamiltonians at different locations.

The powerful inductive biases embedded in CNN architectures, particularly locality and translation equivariance, are pivotal to their efficiency in image processing tasks. They also intrinsically resonate with the fundamental properties and representations of physical many-body systems when dealing with the data at the physical field or spin configuration level.

## B. U-Net Structure

While the inductive biases of locality and translation equivariance make standard CNNs well suited to systems with local interactions, they struggle with long-range correlations near criticality because the receptive field grows only linearly with depth of network. The U-Net architecture [18], built by the encoder and decoder structure, mitigates this by efficiently integrating information across multiple spatial scales, especially when paired with information-preserving resizing (e.g., pixel-shuffle-based rearrangements (see Fig. 12) [29]). Crucially, even when operating on downsampled feature

maps in the encoder that summarize large-scale structure, convolution remains a local operator: kernels still act on neighboring sites of the current lattice, thereby learning transformation rules that are consistent across resolutions—i.e., local physical laws expressed in renormalized coordinates that remain (approximately) scale-invariant. To ensure that the model accurately reflects the underlying physics, we align its architectural choices with the simulation’s boundary conditions. All Monte Carlo simulations in this work employ periodic boundary conditions. Correspondingly, all convolutional layers within the U-Net architecture are implemented with circular padding. This crucial detail enforces the same periodic topology on the feature maps as on the physical lattice, ensuring that the learned local rules are consistent with the system’s global structure.

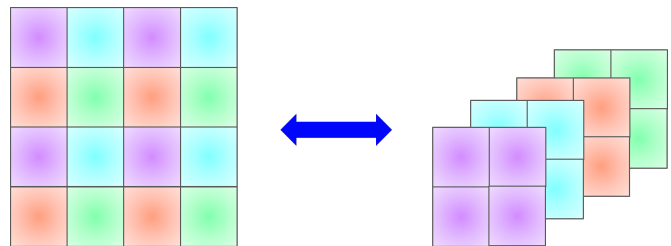


FIG. 12. The pixel shuffle operation [29], a lossless resizing technique used in our U-Net architecture. The encoder employs a space-to-depth pixel shuffle (illustrated from left to right) to downsample spatial resolution while increasing channel depth. Conversely, the decoder uses an inverse depth-to-space pixel shuffle (right to left) for upsampling to reconstruct the spatial dimensions.

Mechanistically, the encoder uses an pixel shuffle (space-to-depth) [29] to reduce spatial resolution without discarding information, mapping, for example, each  $2 \times 2$  block into four channels (see Fig. 12). This preserves translation equivariance and expands the effective receptive field exponentially with depth [30], while convolutions at coarser resolutions still implement local updates on block variables. The decoder applies the inverse pixel shuffle (depth-to-space) to reconstruct high-resolution outputs (see Fig. 12), and skip connections concatenate encoder features with aligned decoder features. This fusion preserves fine-grained locality while enforcing cross-scale consistency, allowing the network to integrate global context without sacrificing the learning of scale-consistent local rules at each resolution. For more architectural and technical details, see the Appendix D.

For many-body physical systems, this design naturally aligns with a renormalization-group perspective: space-to-depth provides a lossless coarse-graining that exposes emergent long-range correlations at the bottleneck, while convolutions at every level learn local interaction laws on the corresponding (reindexed) lattice. Skip connections then reinsert microscopic details, ensuring that global, system-spanning patterns inform but do not overwrite local physics. As a result, U-Net can recognize multi-scale

signatures of criticality while maintaining the learning of (approximately) scale-invariant local physical rules.

To empirically validate that the U-Net’s inductive biases are key to its successful size extrapolation, we conducted a comparative study against a Diffusion Transformer (DiT) model [31], which lacks strong, built-in locality. The U-Net significantly outperformed the DiT, especially in the extrapolation task, despite having substantially fewer parameters. This result supports our claim that architectural alignment with the problem’s local nature is critical. The detailed experimental setup, results, and discussion of this comparison are presented in Appendix E.

### C. Learning Local Physics Instead of Global Statistics

The MCMC simulation is inherently tied to the global parameters of the system it simulates. It learns nothing beyond the equilibrium properties of the size and temperature of that single system. The process is a powerful tool for the analysis of a fixed system, not for learning generalizable physical principles across scales. In contrast, Flow Matching operates on a different principle. It does not sample a stationary distribution but instead learns a deterministic, non-equilibrium transformation. The goal is to construct a continuous path that transforms a simple, unstructured probability distribution (e.g., Gaussian noise) into the complex target data distribution (in our case, the physical spin configurations from MCMC). The characteristics of the Flow Matching Markov process are:

1. **Directed Dynamics** : The process is governed by an ODE defined by a learned vector field. This vector field acts as a time-dependent force that deterministically “flows” any initial random state  $\mathbf{x}_0$  at time  $t = 0$  to a structured, physical state  $\mathbf{x}_1$  at time  $t = 1$ . Unlike MCMC, this process is explicitly designed to change the probability distribution over time, moving it along a predefined path from noise to data.
2. **Learning Local Rules of Transformation** : The model is trained to minimize the discrepancy between its vector field and a target vector field derived from the MCMC data. Crucially, the model is not learning the global statistical properties of the small training systems. Instead, it is learning a function that dictates, for any given configuration  $\mathbf{x}_t$  at any intermediate time  $t$ , the optimal infinitesimal change required to make it more “physics-like.” For the XY model, this involves learning local rules, such as encouraging adjacent spins to align to lower the energy or resolving topological defects like vortices.
3. **Distillation of Scale-Invariant Principles**: The Hamiltonian of the XY model is defined by

local, nearest-neighbor interactions. The physical principles governing low-energy configurations, the preference for smooth spin variations and the structure of vortices, are therefore local and independent of the overall system size. Flow Matching, by learning the vector field from local configuration data, distills these scale-invariant physical rules. Powered by the inductive biases embedded in CNN architectures, the learned vector field at specific site effectively only “sees” the configuration of its local neighborhood, not the global lattice boundaries.

The origin of system-size generalization is that Flow Matching learns local, scale-invariant physics rather than global, size-specific statistics. In contrast to MCMC—which, for a fixed lattice (e.g.,  $32 \times 32$ ), explores the entire equilibrium manifold without embedding knowledge that transfers directly to a larger lattice (e.g.,  $128 \times 128$ )—Flow Matching discovers a continuous representation of the local laws governing spin interactions. Because these laws are local and translationally invariant, the learned vector field effectively acts on small spin patches and is intrinsically agnostic to the global size of the system.

Consequently, applying the trained model to a larger lattice does not extrapolate global statistical properties; it simply deploys the same learned local rules over a broader domain. The model generates valid large-scale configurations because the underlying physics it has internalized is the same at all scales. In essence, the generative model did not learn what a small XY system *looks like*; it learned what the XY model *is* at a fundamental, local level, thereby enabling the construction of physically plausible configurations of arbitrary size.

## IX. DISCUSSION

### A. Comparison of Normalized Flow and Flow Matching

Both Normalizing Flows (NFs) and Flow Matching (FM) are powerful generative frameworks designed to learn a transformation between a simple, tractable base distribution and a complex target data distribution. However, they differ fundamentally in their approach, leading to significant implications for model architecture, training stability, and flexibility (see Fig. 13).

Normalizing Flows construct this transformation as a sequence of invertible and differentiable mappings. This framework’s core requirement is that each transformation’s Jacobian determinant must be computationally tractable. This is essential because NFs rely on the change of variables formula to compute the target distribution’s exact likelihood, which is typically used to minimize the Kullback-Leibler (KL) divergence during training. This constraint imposes severe restrictions on the neural network architectures that can be employed.

To ensure a tractable Jacobian, NFs often utilize specialized structures like coupling layers [32, 33], which partition the input dimensions into active and passive sets. Consequently, these models require carefully designed problem-specific masking mechanisms to ensure that all dimensions are updated over a sequence of layers. This architectural rigidity makes the implementation more complex and potentially unstable, and may also break the inherent symmetries of the modeled system [34, 35], a significant drawback in physical applications.

Flow Matching, on the other hand, circumvents these limitations by reframing the problem. Instead of learning a series of discrete, invertible maps, FM learns the continuous-time vector field—the generator—of a probability flow that transports the base distribution to the target distribution. The model is trained via a straightforward regression objective: minimizing the mean squared error between the network’s predicted vector field and a target vector field derived from simple interpolations between noise and data. Since this process does not require the computation of Jacobian determinants during training, it is free from the rigid architectural constraints that limit NFs. This allows highly flexible and powerful architectures, such as the U-Net employed in this work, without the need for intricate masking schemes or concerns about invertibility. The resulting training process is typically more stable and scalable, highlighting a key advantage of FM in building robust and generalizable generative models. By focusing on learning the flow generator, FM provides a more direct and versatile framework, which we will discuss further.

## B. Generator Learning Framework

Learning the generator in Flow Matching methods, specifically the velocity field along the probability path connecting different distributions, provides numerous advantages. By explicitly modeling this generator through a neural network, the mapping between distributions becomes transparent and interpretable, circumventing the opaque and implicit representations typically encountered in conventional neural networks. This explicit representation significantly improves the flexibility and applicability of the neural network model. Suppose that we treat the neural network as the generator of the distribution mapping, it becomes feasible to employ diverse training strategies beyond Flow Matching alone, such as traditional maximum likelihood estimation or reverse KL divergence minimization in training Normalizing Flows (but need to solve the probability flow ODE during the training process), which can also be adapted to suit various problem contexts and specific research objectives. Overall, this approach aligns well with contemporary efforts in machine learning to build more interpretable, flexible, and versatile generative models, enabling clearer insight into the learned representations and improving

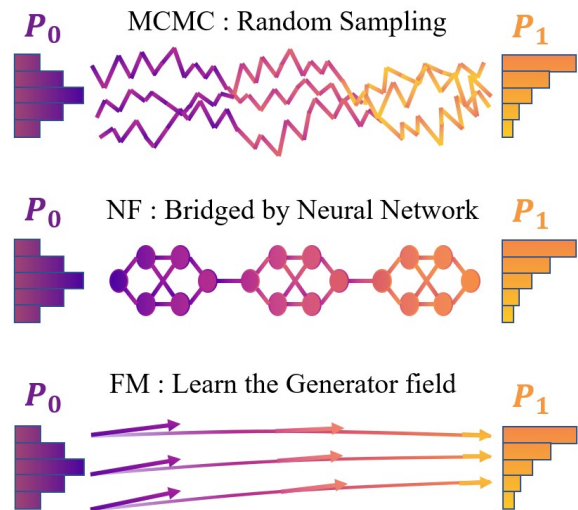


FIG. 13. A schematic comparison of three sampling methodologies. Traditional Markov Chain Monte Carlo (MCMC) operates by randomly sampling configurations from a system’s phase space according to probability weights, a process that can be computationally intensive. Normalizing Flows (NFs) offer a generative alternative by constructing a sequence of invertible maps, but their reliance on a tractable Jacobian determinant imposes significant constraints on the neural network architecture. In contrast, Flow Matching (FM), the approach used in this work, directly learns the vector field (flow) that generates the transformation between distributions. This allows for greater architectural flexibility and a more stable training objective, as samples are transported deterministically along a predefined path.

the model’s adaptability across a broader range of applications.

## C. Limitations of Flow Matching

A significant limitation highlighted by our analysis is the model’s reduced accuracy in predicting second-moment observables, which are directly related to physical fluctuations. This is evident in the increased MSE for susceptibility as system size grows (see Fig. 9) and, more strikingly, in the statistical noise observed in the extrapolated spin stiffness, as detailed in Appendix C. This behavior is likely rooted in the nature of the regression-based training objective (Eq. 10), which excels at learning the mean of the conditional velocity field but may under-represent its complete variance. This characteristic in fact constrains the direct application of this framework to physical problems where high-precision information about fluctuations, such as calculating critical exponents from specific heat or susceptibility, is paramount. Improving the model’s ability to capture the variance of the target distribution faithfully is therefore a critical challenge for future research. Potential avenues could include exploring alternative loss functions that are more

sensitive to higher-order moments of the distribution, or incorporating iterative refinement schemes during inference to better sample the whole configuration space.

Another limitation is that the Flow Matching framework is designed for systems with continuous degrees of freedom, as in the XY model. Its extension to discrete models (e.g., Ising or Potts) is non-trivial, as the continuous probability flow is not directly applicable. There are two main paths to address this challenge. The first involves reformulating the discrete problem into an equivalent continuous one, for instance, using an auxiliary field method like the Hubbard-Stratonovich transformation, making the system tractable for our approach. A second, more direct path is to leverage generative models explicitly designed for discrete spaces. The development of frameworks such as Masked Diffusion [36] and more recent Discrete Flow Matching [37] marks a promising research frontier for applying these powerful sampling techniques to a broader class of physical systems. Indeed, several recent works have already started to explore such applications [38].

## X. CONCLUSION AND OUTLOOK

In this work, we have introduced a generative model based on Flow Matching that represents a new paradigm for the computational study of many-body systems. Our key finding is that a single network, by learning the scale-invariant, local physical rules of the Hamiltonian rather than the global statistics of a specific system size, can generate high-fidelity configurations across continuous temperatures and, crucially, for significantly larger lattices. This dual-generalization capability fundamentally alters the workflow for studying critical phenomena. It replaces the traditional, brute-force approach of running separate, costly simulations for each system size with a more efficient "train-small, predict-large" strategy. As our analysis shows, this approach provides a significant net computational advantage for large-scale studies, making robust finite-size scaling analysis more accessible.

The principles underpinning this method's success—aligning the inductive biases of a CNN architecture with the locality inherent in physical Hamiltonians—suggest its applicability to a broader class of models. The framework is particularly well-suited for systems described by continuous fields on a lattice, opening promising avenues for its application in lattice field theories, such as scalar  $\phi^4$  theory. Furthermore, its utility could extend to quantum many-body problems, especially those where quantum Monte Carlo methods map the system onto a classical statistical model with continuous variables. This work thus establishes a reliable and computationally superior methodology for exploring the thermodynamic limit and provides a flexible foundation for future explorations in statistical mechanics and beyond.

## XI. ACKNOWLEDGMENT

We thank Chi-Ting Ho, Hsuan-Yu Wu, and Po-Chung Chen for valuable discussions. This work is supported by the National Center for Theoretical Sciences, the Higher Education Sprout Project funded by the Ministry of Science and Technology, and the Ministry of Education in Taiwan. DWW is supported under the grant NSTC 113-2112-M-007-036.

### Appendix A: Details of Loss Function

In Eq (10) which we can show that the gradient is same as in Eq (9):

$$\begin{aligned} \nabla_{\theta} \mathcal{L}_{FM} &= \int_0^1 dt \int [\mathcal{D}\mathbf{x}_t] p_t(\mathbf{x}_t) \nabla_{\theta} [\mathbf{v}_{\theta}^2 - 2\mathbf{v}_{\theta} \cdot \mathbf{u}_t] \\ &= \int_0^1 dt \int [\mathcal{D}\mathbf{x}_0 \mathcal{D}\phi] \nabla_{\theta} [p_t(\mathbf{x}_t|\phi) q(\phi) \mathbf{v}_{\theta}^2 \\ &\quad + 2\mathbf{v}_{\theta} \cdot \mathbf{v}_t(\mathbf{x}_t|\phi) p_t(\mathbf{x}_t|\phi) q(\phi)] \\ &= \nabla_{\theta} \mathcal{L}_{CFM} \end{aligned} \quad (\text{A1})$$

However, it is numerically difficult to calculate the loss function  $\mathcal{L}(\theta)$  in Eq. (10) directly. Thus, the strategy is to sample few pairs of  $(\mathbf{x}_0, \mathbf{x}_1)$  and other conditions randomly in each training step, calculate the corresponding  $\mathbf{x}_t$ , and minimize  $[\mathbf{v}_{\theta}(\mathbf{x}_t, t|\phi) - \mathbf{v}_t(\mathbf{x}_t|\phi)]^2$  by updating the parameters  $\theta$ . After repeating the above steps until the neural network converges, we can use learned neural network  $\mathbf{v}_{\theta}(\mathbf{x}_t, t|\phi)$  to approximate velocity field  $\mathbf{u}_t(\mathbf{x}_t)$ . Now the loss function is the expectation value that can be written as

$$\begin{aligned} \mathcal{L}_{CFM}(\theta) &= \\ \mathbb{E}_{(\mathbf{x}_1, \phi) \sim \mathcal{P}_{data}, \mathbf{x}_0 \sim \mathcal{N}(0, I), t \sim p(t)} &[\mathbf{v}_{\theta}(\mathbf{x}_t, t|\phi) - (\mathbf{x}_1 - \mathbf{x}_0)]^2 \end{aligned} \quad (\text{A2})$$

Here, the distribution of time  $p(t)$  can be chosen as uniform between 0 and 1. But the better choice of  $p(t)$  will be discussed in the next section.

### Appendix B: Training and Sampling Strategy

According to the path defined in Eq. (1), we can define the effective signal-to-noise ratio (SNR) and the logarithm SNR ( $\lambda(t)$ ) as

$$SNR \equiv \frac{t^2}{(1-t)^2}, \quad \lambda(t) \equiv \log SNR = 2 \text{logit}(t) \quad (\text{B1})$$

Experience has revealed that Flow Matching will have a relatively large error when the SNR is 1, so sampling

time from a logit normal distribution in Eq. (B2) with  $\mu = 0$  and  $\sigma = 1$  during the training phase would be a good choice.[39]

$$p(t, \mu, \sigma) \equiv \frac{1}{\sigma\sqrt{2\pi}} \frac{1}{t(1-t)} \exp\left(-\frac{(\text{logit}(t) - \mu)^2}{2\sigma^2}\right) \quad (\text{B2})$$

Since the curvature of the probability flow ODE solution is inconsistent at different times (see Fig. 2). By mapping the time steps, reducing the time-step spacing where the curvature is large and enlarging the time step spacing where the curvature is slight can achieve better sampling quality. Since the time is sampled from the logit normal distribution during the training phase, the log-SNR  $\lambda(t)$  in Eq. (B1) can be reparameterized with a new mean and standard deviation  $\lambda(t, \mu, \sigma)$ ,

$$\lambda(t, \mu, \sigma) \equiv 2(\mu + \sigma \text{logit}(t)) \quad , \quad \text{logit}(t) \sim \mathcal{N}(0, 1) \quad (\text{B3})$$

and the corresponding time-mapping relationship can be solved as

$$\lambda(t, \mu, \sigma) = \lambda(t') \Rightarrow t'(t, \mu, \sigma) = \frac{e^\mu}{e^\mu + (\frac{1}{t} - 1)\sigma} \quad (\text{B4})$$

The advantage of this time schedule is that one can flexibly adjust the mean and standard deviation to adapt to different sampling situations, and it is an effective means in practice.[39][40] In this work, the  $(\mu, \sigma)$  are set to  $(0, 1)$  during training phase and  $(-0.3, 1)$  during inference phase.

All models in this work were trained using an identical hyperparameter configuration. We employed the AdamW optimizer [41] with the 1-cycle learning rate policy [42], setting the maximum learning rate to  $2 \times 10^{-4}$ . Training was conducted with a batch size of 32, and we used 4 steps of gradient accumulation, resulting in an effective batch size of 128 for each parameter update.

The training and inference process is detailed in Algorithms 1 and 2. The  $\mathbf{x}_1$  is the spin configuration (spin angles) generated by the MCMC,  $\mathbf{x}_0$  is the standard Gaussian noise with the same shape of spin configuration,  $c_{\text{data}}$  is the corresponding temperature of the spin configuration and  $p_t(t, \mu, \sigma)$  is the logit normal distribution in Eq. (B2). In the inference stage, since the probability flow ODE needs to be solved, the computational accuracy and time cost must be considered at the same time. On the premise that Flow Matching maintains the efficiency advantage over traditional algorithms, the 3rd-order Heun's (Heun3) method within 10 steps is reliable. All Flow Matching sampling methods in this work use the 5-step Heun3 method to sample spin configurations.

---

**Algorithm 1: Flow Matching — Training**


---

**Input:** Prior distribution  $\mathcal{N}(0, \mathbb{I})$ , time distribution  $p(t, \mu, \sigma)$ , data distribution  $p_{\text{data}}$ , conditioning data  $c_{\text{data}}$ , velocity field model  $\mathbf{v}_\theta$ , number of training steps  $N$ , batch size  $B$ , learning rate  $\eta$

**Output:** Trained model parameters  $\theta$

**for**  $n \leftarrow 1$  **to**  $N$  **do**

- Sample  $(\mathbf{x}_1, c) \sim (p_{\text{data}}^B, c_{\text{data}}^B)$
- Sample  $\mathbf{x}_0 \sim \mathcal{N}^B(0, \mathbb{I})$
- Sample  $t \sim p^B(t, \mu, \sigma)$
- $\mathbf{x}_t \leftarrow t\mathbf{x}_1 + (1-t)\mathbf{x}_0$  **Conditional flow path**
- $\mathbf{v}_\star \leftarrow \mathbf{x}_1 - \mathbf{x}_0$  **Conditional vector field target**
- $\mathcal{L} \leftarrow \frac{1}{B} \sum_{i=1}^B \|\mathbf{v}_\theta(\mathbf{x}_t^{(i)}, t^{(i)}, c^{(i)}) - \mathbf{v}_\star^{(i)}\|_2^2$
- $\theta \leftarrow \theta - \eta \nabla_\theta \mathcal{L}$  **Update model parameters**

**return**  $\theta$

---



---

**Algorithm 2: Flow Matching — Inference with Time-Mapping and 3rd-Order Heun's Method**


---

**Input:** Prior distribution  $\mathcal{N}(0, \mathbb{I})$ , velocity field  $\mathbf{v}_\theta$ , number of steps  $K$ , conditioning  $c_{\text{data}}$ , time-mapping function  $t'(\cdot, \mu, \sigma)$

**Output:** Sample  $\mathbf{x}_K \approx p_{\text{data}}$

Sample  $\mathbf{x}_0 \leftarrow \mathcal{N}(0, \mathbb{I})$

Generate uniform time steps  $\tau_k = k/K$  for  $k = 0, \dots, K$

Map to non-uniform time steps  $t_k = t'(\tau_k, \mu, \sigma)$  for  $k = 0, \dots, K$

**for**  $k \leftarrow 0$  **to**  $K - 1$  **do**

- $h \leftarrow t_{k+1} - t_k$  **Non-uniform step size**
- $\mathbf{k}_1 \leftarrow \mathbf{v}_\theta(\mathbf{x}_k, t_k, c_{\text{data}})$
- $\mathbf{k}_2 \leftarrow \mathbf{v}_\theta(\mathbf{x}_k + \frac{h}{3}\mathbf{k}_1, t_k + \frac{h}{3}, c_{\text{data}})$
- $\mathbf{k}_3 \leftarrow \mathbf{v}_\theta(\mathbf{x}_k + \frac{2h}{3}\mathbf{k}_2, t_k + \frac{2h}{3}, c_{\text{data}})$
- $\mathbf{x}_{k+1} \leftarrow \mathbf{x}_k + \frac{h}{4}(\mathbf{k}_1 + 3\mathbf{k}_3)$

**return**  $\mathbf{x}_K$

---

**Appendix C: More Physics Observables in Size Extrapolation**

To provide a comprehensive view of the model's extrapolation performance, this appendix presents a detailed comparison for several key observables across system sizes  $L = 16, 32, 64,$  and  $128$ . The model was trained only on  $L = 32$  data with 1500 configurations per temperature from MCMC. The setup is identical to Sec. V. The results distinguish between the model's robust performance on first-moment quantities (energy, vortex density) and its challenges with the second-moment, fluctuation-related quantity (spin stiffness).

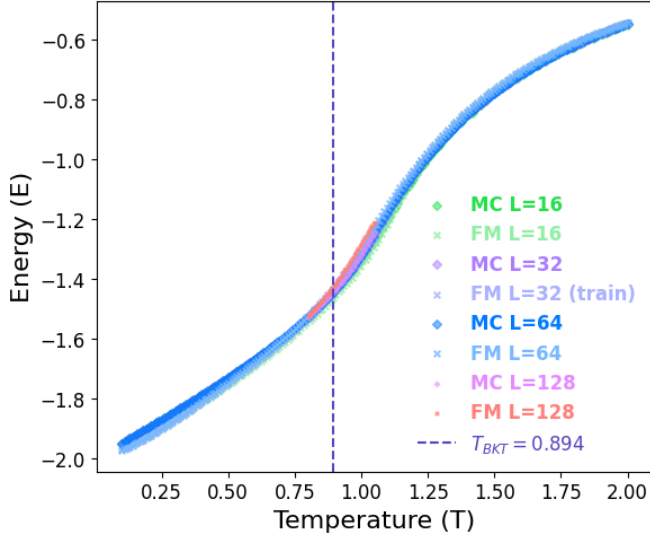


FIG. 14. Size extrapolation of energy per site  $E(T)$  for various system sizes ( $L = 16, 64, 128$ ). A single Flow Matching (FM) model, trained only on  $32 \times 32$  data, generates configurations that show excellent agreement with the reference MCMC (MC) data. This highlights the model’s ability to accurately extrapolate first-moment quantities.

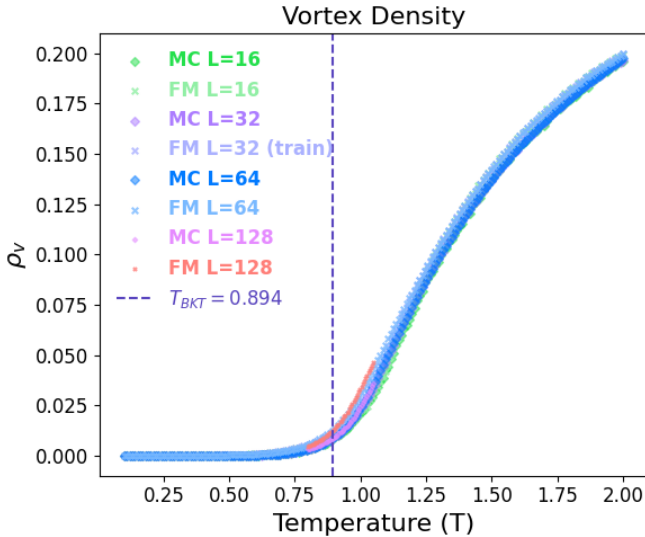


FIG. 15. Size extrapolation of vortex density  $\rho_v(T)$  for various system sizes ( $L = 16, 64, 128$ ). Generated by a single Flow Matching (FM) model trained only on  $32 \times 32$  data, the results align well with the MCMC (MC) reference. This further validates the model’s robust performance on observables not primarily driven by large-scale fluctuations.

#### Appendix D: Neural Network Architecture

Our model employs a U-Net architecture, a design renowned for its efficacy in image-to-image tasks due to its hierarchical structure that captures multi-scale features [18]. The network is composed of an encoder path,

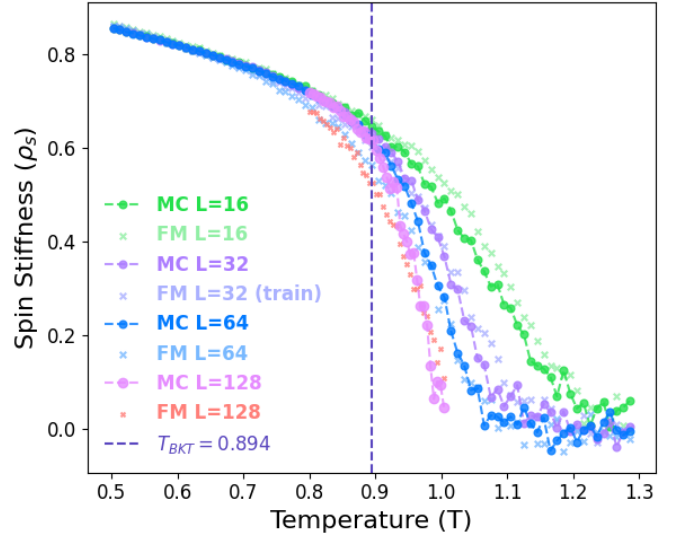


FIG. 16. Size extrapolation of spin stiffness  $\rho_s(T)$  for various system sizes ( $L = 16, 64, 128$ ), generated from a single FM model trained on  $32 \times 32$  data. The statistical noise visible across all curves, including the MCMC (MC) reference, is partially attributable to the modest ensemble size of 1500 configurations per temperature used for both training and comparison. While the FM model captures the qualitative behavior, a rigorous finite-size scaling analysis for the BKT transition requires locating the intersection of the stiffness curve with the universal line  $2T/\pi$ , according to the Nelson-Kosterlitz criterion [43]. As the figure shows, for extrapolated sizes ( $L = 64, 128$ ), a noticeable deviation between the FM and MC results appears near the critical transition temperature where this intersection is expected. This discrepancy invalidates a scaling analysis based on the intersection point and justifies our choice to use the more robust susceptibility peak (Sec. V).

a bottleneck, and a decoder path, with skip connections linking corresponding levels of the encoder and decoder to preserve high-resolution spatial details. To handle the conditional nature of our generation task, the model integrates time and temperature embeddings, which are processed and fused before modulating the network’s behavior at each block.

#### 1. Core Building Blocks

The fundamental component of our U-Net is the “ResnetBlock” (RB). Each block consists of two main sequential operations: a spatial processing layer and a feedforward neural network. The input to each operation is first normalized using Root Mean Square Layer Normalization, a variant of Layer Normalization known for its computational efficiency and performance [44].

A key feature of the RB (see Fig. 17) is its adaptive conditioning mechanism, inspired by the Adaptive Layer Normalization (adaLN) used in Diffusion Trans-

formers [31]. The conditional embedding, derived from time and temperature, is passed through a linear layer to generate shift and scale parameters. These parameters modulate the normalized feature maps within the block, allowing the network’s behavior to be dynamically controlled by the input conditions.

While the U-Net’s convolutional layers excel at learning local physical rules due to their inherent inductive biases of locality and translation equivariance, they are less effective at capturing the long-range correlations that emerge near critical points. To address this limitation, we replace the standard convolutional layers in RB with a specialized multi-head self-attention mechanism [45] in the network’s deeper, lower resolution levels. The structure is shown in Fig. 17, which is denoted as ”Resnet-Block (Attention)” (RBA) in the figure.

This attention mechanism incorporates a learnable 2D Rotary Position Embedding (RoPE), which has demonstrated a remarkable ability to handle multi-scale inputs and extrapolate across resolutions [46]. By applying rotational transformations to the query and key vectors based on their spatial coordinates, 2D RoPE effectively encodes relative positional information directly into the attention mechanism. This allows the model to capture complex, long-range dependencies between spin sites across the entire lattice, a crucial capability for modeling systems at or near a phase transition where correlation lengths diverge. The frequencies of the rotary embeddings are treated as learnable parameters, enabling the model to adapt the positional encoding to the specific physics of the system.

## 2. Optimization of Neural Network Architecture

The entire model is optimized using ”torch.compile” to enhance computational efficiency [47]. For certain blocks (”ResnetBlock” and ”ResnetBlock (Attention)” in Fig. 17) in model is optimized using ”epilogue fusion” and ”max autotune” supported by PyTorch [47] to perform operator fusion automatically. Please refer to the code in the following link for the detailed structure of the neural network. (<https://github.com/ToelUl/Flow-U-Net>)

### Appendix E: Comparison between U-Net and DiT Architectures

To show that the inductive biases embedded in CNN architectures of U-Net are the key point for training on data of a fixed system size and extrapolating to other sizes, we compare the results using another robust neural network architecture: the Diffusion Transformer [31].

Vision Transformers [48] and, by extension, the Diffusion Transformer (DiT) [31] variants recently adopted for generative modeling, rely on minimal inductive biases. Transformer’s core is the self-attention mechanism [45]. This mechanism empowers them with global receptive fields and permutation equivariance, enabling each image

patch (or token) to interact with all others regardless of spatial proximity. The only explicit inductive bias is introduced through the positional encoding scheme, which merely injects order information rather than enforcing locality. As a consequence, Transformers excel when long-range correlations or nonlocal dependencies dominate the target distribution, conditions frequently encountered in natural language, graphs, and physical systems near criticality where correlation lengths diverge. But in our case, the underlying data-generating process is governed by a physical Hamiltonian with strictly local interactions.

We conducted a comparative experiment under identical training conditions to validate this hypothesis. Both the U-Net and DiT models were trained on the same dataset from MCMC simulations of a  $32 \times 32$  system. Notably, to specifically accommodate the potentially higher data requirements of the larger DiT model, we increased the number of training samples to 2500 configurations per temperature point (up from 1500 used in the system size extrapolation experiment, see Sec. V). Both models were trained for the same number of epochs with an identical optimizer and learning rate schedule, ensuring a controlled comparison. Both models ensure that the training has converged and the training loss curve is shown in the Fig. 18.

A potential concern in this comparison is the significant disparity in model size (Table I), where the DiT model has nearly six times more parameters than the U-Net. One might argue that the DiT’s poorer performance could stem from a larger, more complex model that is inherently more difficult to train, rather than from a fundamental misalignment of its inductive biases.

TABLE I. Comparison of U-Net and DiT model architectures. Due to its structural limitations, the DiT model is significantly larger regarding parameters and computational cost (floating point operations, FLOPs). All training and inference conditions were held constant between the two models.

Metric	U-Net	DiT
Parameters	214.65 K	1262.98 K
FLOPs	0.9776 G	6.4847 G
Memory (params)	0.82 MB	4.82 MB

However, we argue that this disparity in parameters is not a confounding factor but a direct consequence of the architectural differences and is, in fact, central to our conclusion. The DiT architecture, lacking a built-in locality bias, requires a much larger parameter space to learn local physical relations from data—a task for which the U-Net is purpose-built via its convolutional structure. The DiT’s substantial parameter count is a necessity from its lack of correct inductive bias. Therefore, its struggle to train effectively under these conditions is not an artifact of an unfair comparison but rather a direct demonstration of our central thesis: for physical systems governed by local interactions, having the correct architectural inductive bias is far more critical than raw model capacity. The training challenge itself highlights the inherent effi-

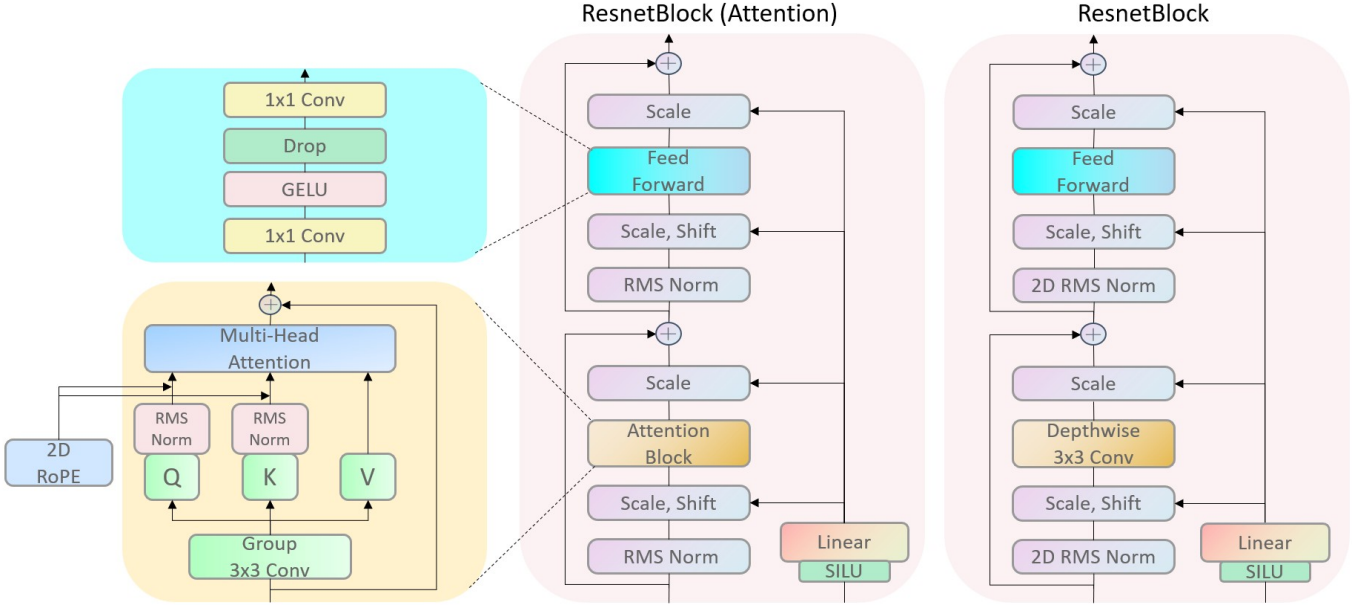


FIG. 17. The core Building Blocks in U-Net. The left-hand side is "ResnetBlock (Attention)" (RBA), which is used in the network's deeper, lower resolution levels. "ResnetBlock" (RB) and "ResnetBlock (Attention)" (RBA) share the same structure except for the attention block. Please refer to the code in the following link for the detailed structure of the neural network. (<https://github.com/ToelU1/Flow-U-Net>)

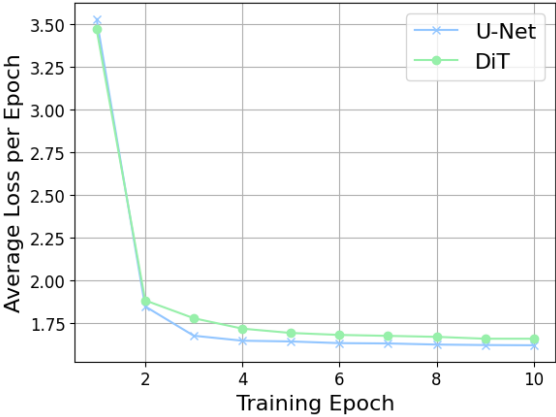


FIG. 18. Training loss curves of U-Net and DiT, where each point represents the average loss per epoch. The two models exhibit similar convergence behavior, but U-Net performs better. Inference sampling results for the two models are shown in Figs. 19 and 20.

ciency and superiority of the U-Net's architecture for this class of problems.

The DiT architecture, lacking strong locality bias, must deduce the principle of locality entirely from the training data. Its self-attention mechanism initially treats all pairs of sites as potentially relevant, placing a significant learning burden on the model to discover that the system's dynamics are overwhelmingly dominated by nearest-neighbor interactions. This leads to a critical challenge in generalization, as observed in our

Flow Matching experiments (see Figs. 19 and 20). The DiT model tends to learn correlations and patterns that are specific to the fixed system size seen during training, rather than the universal, size-invariant rule of local physical law. When extrapolating to larger, unseen system sizes ( $64 \times 64$ ), the global attention patterns learned in the smaller system are no longer directly applicable, leading to a significant performance degradation.

Conversely, the powerful inductive biases of a CNN-based architecture in the U-Net align perfectly with the fundamental structure of the local Hamiltonian. The convolutional kernel intrinsically learns a local rule that is, by its very nature, independent of the total system size. This inherent understanding of locality and translation equivariance means the learned physical principles are more robust and readily generalizable. The network does not need to waste capacity learning the concept of locality; it can instead focus on modeling the specific nature of these local interactions. This alignment explains why the U-Net architecture demonstrates superior extrapolation capabilities, successfully generalizing to different system sizes after being trained on only one.

This observation is consistent with a large body of literature in computer vision comparing Transformers and CNNs. The seminal work on Vision Transformers by Dosovitskiy et al. [48] explicitly states that Transformers lack the inductive biases of locality and translation equivariance, making them heavily reliant on massive-scale pre-training to generalize effectively. Subsequent analyses, such as the work by Raghu et al. [49], have provided further evidence, showing that ViTs must learn to

represent local information from scratch, a task for which CNNs are architecturally predisposed. Our comparative experiment with the DiT model, therefore, serves as a direct demonstration of this principle within a physical simulation context: the model with the correct inductive bias (U-Net) not only performs better but does so with a fraction of the parameters, because its architecture is already aligned with the fundamental, local nature of the physical system.

## Appendix F: GPU-accelerated Monte Carlo Method

We employ a highly optimized MCMC simulation framework implemented in PyTorch [47]. The full implementation of our algorithm is available on GitHub: (<https://github.com/ToelUL/Thermal-Phase-Transition-MC-GPU-Simulation>).

The algorithm is designed to leverage the massively parallel architecture of modern Graphics Processing Units (GPUs), enabling large-scale simulations with high statistical precision. The core design incorporates three key parallelization strategies: a checkerboard update scheme for intra-lattice parallelism, the simulation of multiple independent Markov chains, and the replica-exchange method (also known as Parallel Tempering) across a range of temperatures.

### 1. Parallel Architecture and Data Layout

The fundamental data structure for the spin configurations is a four-dimensional tensor of shape  $B \times C \times L \times L$ , where:

- $B$  is the batch size, representing the number of different temperatures simulated simultaneously.
- $C$  is the number of independent Monte Carlo chains for each temperature.
- $L$  is the linear size of the square lattice.

This layout allows for all temperatures and chains to be processed in parallel. Operations are vectorized across the first two dimensions ( $B$  and  $C$ ), which maps naturally to the single instruction, multiple data (SIMD) paradigm of GPU computing. The use of  $C$  independent chains per temperature not only accelerates the accumulation of statistics but also enhances the statistical independence of the collected samples, providing a more robust ensemble average.

### 2. Checkerboard Metropolis-Hastings Update

A standard single-spin flip Metropolis-Hastings algorithm introduces data dependencies, as the update of a spin requires knowledge of its neighbors, precluding simultaneous updates of adjacent spins. To overcome this

limitation and maximize parallel efficiency, we implement a **checkerboard update scheme** [50]. The lattice is decomposed into two independent sub-lattices, 'A' and 'B' (analogous to the black and white squares of a checkerboard).

A single Monte Carlo sweep consists of two sequential steps:

1. All spins on sub-lattice A are updated simultaneously. Since no spin on sub-lattice A is a nearest neighbor to any other spin on A, these updates are fully independent and can be performed in a single, vectorized operation on the GPU.
2. All spins on sub-lattice B are then updated simultaneously in the same manner.

For the XY model, where the Hamiltonian is given by:

$$H = -J \sum_{\langle i,j \rangle} \cos(\theta_i - \theta_j) \quad (\text{F1})$$

the local update involves proposing a new angle  $\theta'_i = \theta_i + \delta\theta$  for a spin  $i$ , where  $\delta\theta$  is a random perturbation. The change in energy,  $\Delta E$ , is computed based only on the local spin and its neighbors. The proposed move is then accepted with the probability:

$$P_{\text{acc}}(\theta_i \rightarrow \theta'_i) = \min\left(1, e^{-\Delta E/T}\right) \quad (\text{F2})$$

where  $T$  is the temperature of the specific replica. This entire process, from proposing moves to accepting them, is executed in parallel for all spins on the active sub-lattice across all chains and temperatures.

### 3. Parallel Tempering (Replica-Exchange)

To mitigate critical slowing down near phase transitions and to ensure efficient exploration of the configuration space, our framework implements the **Parallel Tempering (or replica-exchange) algorithm** [10]. This method involves running simulations at multiple temperatures  $T_1, T_2, \dots, T_B$  in parallel. Periodically, an exchange of the entire spin configurations between two adjacent replicas, say at temperatures  $T_i$  and  $T_{i+1}$  with energies  $E_i$  and  $E_{i+1}$ , is proposed.

The exchange is accepted with a probability that satisfies the detailed balance condition:

$$P(\text{swap}) = \min\left(1, \exp\left[\left(\frac{1}{T_i} - \frac{1}{T_{i+1}}\right)(E_i - E_{i+1})\right]\right) \quad (\text{F3})$$

This allows configurations from high-temperature replicas, which explore the energy landscape more broadly, to diffuse to lower temperatures, preventing them from getting trapped in local energy minima. To ensure detailed balance over the entire system, exchange

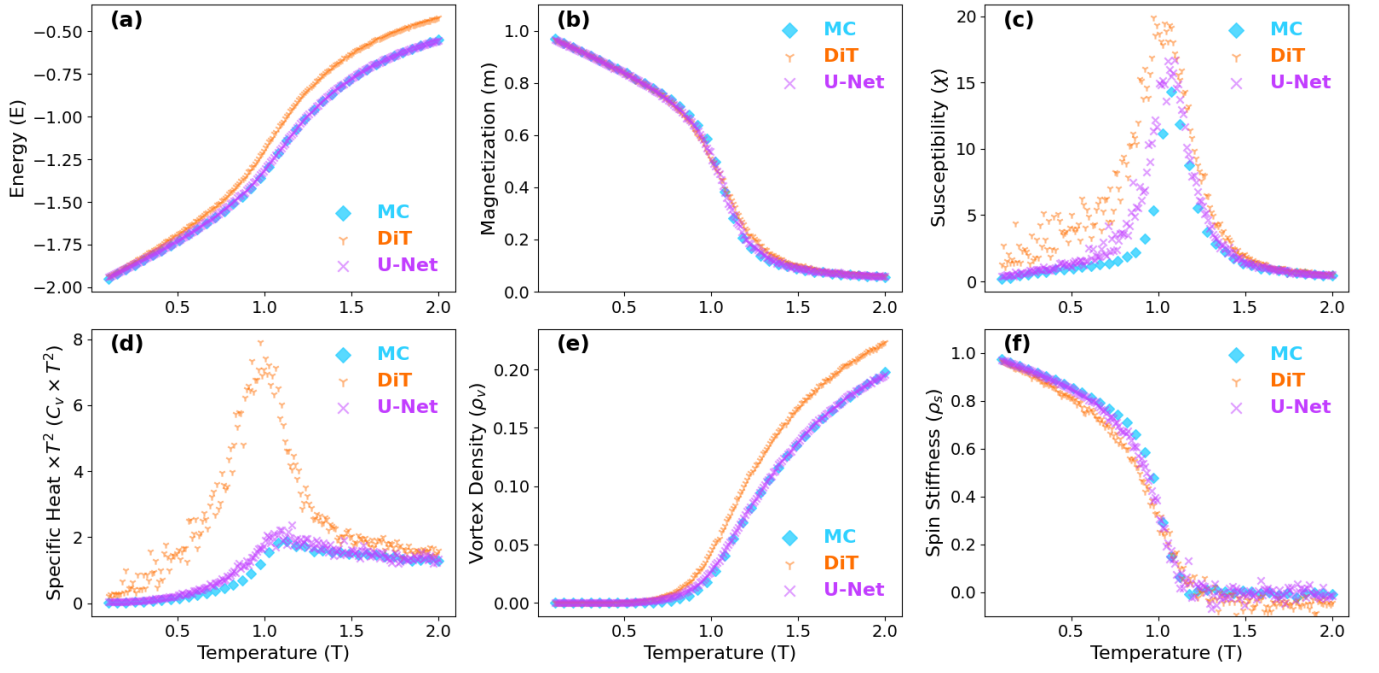


FIG. 19. This figure shows the performance of the U-Net and DiT trained and sampled at the same size ( $32 \times 32$ ). The MCMC (MC) data used for training and comparison have a temperature interval 0.05. The sampling temperature interval of U-Net and DiT after training with Flow Matching is 0.01. The figure clearly shows that even when sampling at the training size, DiT, which lacks the correct inductive bias, cannot learn the correct physical behavior with limited training data like the U-Net.

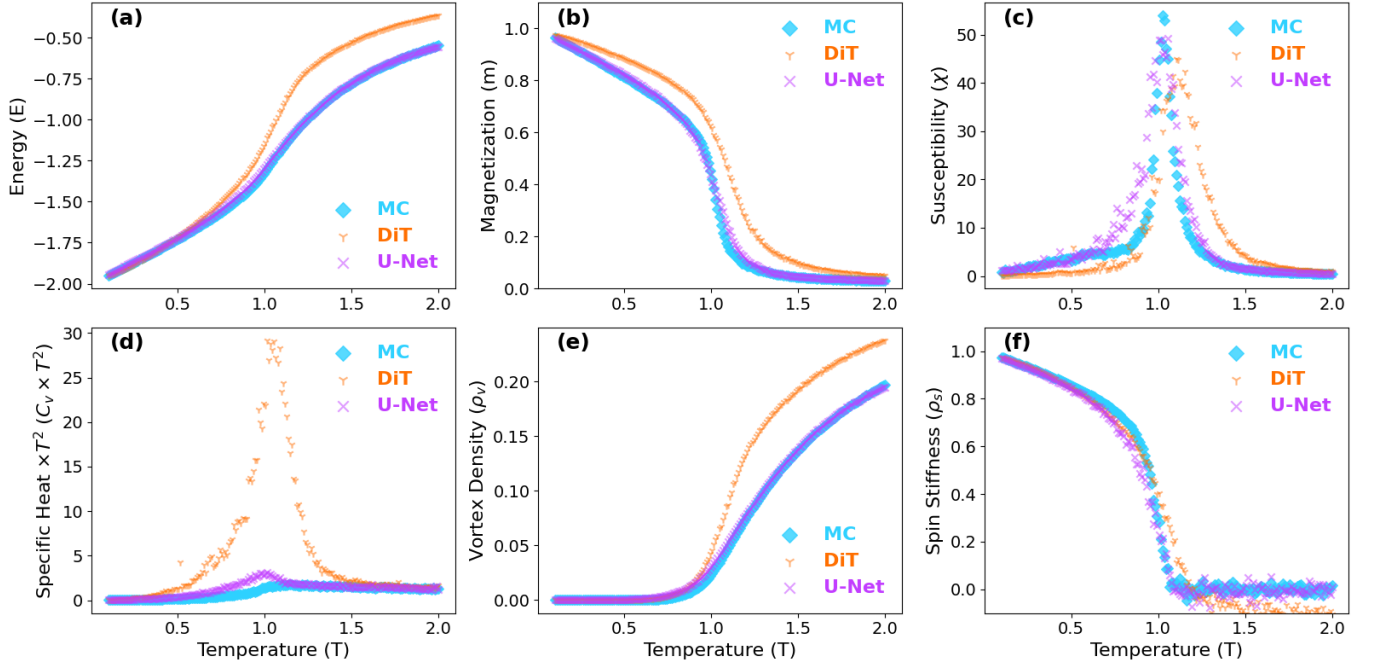


FIG. 20. This figure shows the performance of U-Net and DiT trained at size  $32 \times 32$  and sampled at a larger size  $64 \times 64$ . The MCMC data used for training at size  $32 \times 32$  had a temperature interval of 0.05. U-Net and DiT, after training with Flow Matching, had a sample temperature interval of 0.01. The MCMC (MC) data used for comparison at the larger size  $64 \times 64$  in the figure had a temperature interval of 0.01. The figure shows that DiT, which lacks the correct inductive bias, has worse results under size extrapolation (compared to Figs. 19) and does not exhibit correct finite-size scaling behavior.

attempts are alternated between pairs  $(T_i, T_{i+1})$  with even  $i$  and those with odd  $i$ . This technique significantly

improves the convergence and ergodicity of the simulation, especially for complex systems.

By combining these three levels of parallelism, the algorithm achieves a substantial reduction in simulation time while generating statistically robust and independent samples across a wide range of temperatures.

### Appendix G: Information about Computing Resources.

All numerical experiments, including model training, inference, and Monte Carlo simulations, were conducted on a workstation with the following specifications.

- **CPU:** AMD Ryzen 9 9950X 16-Core Processor
- **GPU:** 1x NVIDIA GeForce RTX 4080 (16 GB VRAM)
- **Operating System:** Windows Subsystem for Linux 2 (WSL2)
- **Core Libraries [22, 47, 51]:**
  - PyTorch: 2.7.1 (+cu128)
  - CUDA Toolkit (used by PyTorch): 12.8
  - cuDNN: 9.7.1
  - flow\_matching: 1.0.10

- 
- [1] D. P. Landau and K. Binder, *A Guide to Monte Carlo Simulations in Statistical Physics*, 2nd ed. (Cambridge University Press, 2005).
- [2] A. W. Sandvik, A. Avella, and F. Mancini, Computational studies of quantum spin systems, in *AIP Conference Proceedings* (AIP, 2010).
- [3] W. M. C. Foulkes, L. Mitas, R. J. Needs, and G. Rajagopal, Quantum monte carlo simulations of solids, *Rev. Mod. Phys.* **73**, 33 (2001).
- [4] A. Bazavov, D. Toussaint, C. Bernard, J. Laiho, C. Detar, L. Levkova, M. B. Oktay, S. Gottlieb, U. M. Heller, J. E. Hetrick, P. B. Mackenzie, R. Sugar, and R. S. Van de Water, Nonperturbative qcd simulations with 2+12+1 flavors of improved staggered quarks, *Rev. Mod. Phys.* **82**, 1349 (2010).
- [5] D. J. E. Callaway and A. Rahman, Microcanonical ensemble formulation of lattice gauge theory, *Phys. Rev. Lett.* **49**, 613 (1982).
- [6] S. Duane, A. Kennedy, B. J. Pendleton, and D. Roweth, Hybrid monte carlo, *Physics Letters B* **195**, 216 (1987).
- [7] U. Wolff, Collective monte carlo updating for spin systems, *Phys. Rev. Lett.* **62**, 361 (1989).
- [8] S. Schaefer, R. Sommer, and F. Vrotta, Critical slowing down and error analysis in lattice qcd simulations, *Nuclear Physics B* **845**, 93–119 (2011).
- [9] M. Troyer and U.-J. Wiese, Computational complexity and fundamental limitations to fermionic quantum monte carlo simulations, *Phys. Rev. Lett.* **94**, 170201 (2005).
- [10] K. Hukushima and K. Nemoto, Exchange monte carlo method and application to spin glass simulations, *Journal of the Physical Society of Japan* **65**, 1604–1608 (1996).
- [11] M. S. Albergo, G. Kanwar, and P. E. Shanahan, Flow-based generative models for markov chain monte carlo in lattice field theory, *Phys. Rev. D* **100**, 034515 (2019).
- [12] D. C. Hackett, C.-C. Hsieh, S. Pontula, M. S. Albergo, D. Boyda, J.-W. Chen, K.-F. Chen, K. Cranmer, G. Kanwar, and P. E. Shanahan, **Flow-based sampling for multimodal and extended-mode distributions in lattice field theory** (2025), [arXiv:2107.00734](https://arxiv.org/abs/2107.00734) [hep-lat].
- [13] A. Singha, D. Chakrabarti, and V. Arora, Conditional normalizing flow for markov chain monte carlo sampling in the critical region of lattice field theory, *Phys. Rev. D* **107**, 014512 (2023).
- [14] M. Gerdes, P. de Haan, C. Rainone, R. Bondesan, and M. C. N. Cheng, Learning lattice quantum field theories with equivariant continuous flows, *SciPost Physics* **15**, 10.21468/scipostphys.15.6.238 (2023).
- [15] K. A. Nicoli, C. J. Anders, T. Hartung, K. Jansen, P. Kessel, and S. Nakajima, Detecting and mitigating mode-collapse for flow-based sampling of lattice field theories, *Phys. Rev. D* **108**, 114501 (2023).
- [16] L. Wang, G. Aarts, and K. Zhou, Diffusion models as stochastic quantization in lattice field theory, *Journal of High Energy Physics* **2024**, 60 (2024).
- [17] K. Fukushima and S. Kamata, Stochastic quantization and diffusion models, *Journal of the Physical Society of Japan* **94**, 10.7566/jpsj.94.031010 (2025).
- [18] O. Ronneberger, P. Fischer, and T. Brox, **U-net: Convolutional networks for biomedical image segmentation** (2015), [arXiv:1505.04597](https://arxiv.org/abs/1505.04597) [cs.CV].
- [19] Y. Lipman, R. T. Q. Chen, H. Ben-Hamu, M. Nickel, and M. Le, **Flow matching for generative modeling** (2023), [arXiv:2210.02747](https://arxiv.org/abs/2210.02747) [cs.LG].
- [20] Y. Song, J. Sohl-Dickstein, D. P. Kingma, A. Kumar, S. Ermon, and B. Poole, **Score-based generative modeling through stochastic differential equations** (2021), [arXiv:2011.13456](https://arxiv.org/abs/2011.13456) [cs.LG].
- [21] J. Ho, A. Jain, and P. Abbeel, **Denoising diffusion probabilistic models** (2020), [arXiv:2006.11239](https://arxiv.org/abs/2006.11239) [cs.LG].
- [22] Y. Lipman, M. Havasi, P. Holderrith, N. Shaul, M. Le, B. Karrer, R. T. Q. Chen, D. Lopez-Paz, H. Ben-Hamu, and I. Gat, **Flow matching guide and code** (2024), [arXiv:2412.06264](https://arxiv.org/abs/2412.06264) [cs.LG].
- [23] Z. Geng, M. Deng, X. Bai, J. Z. Kolter, and K. He, **Mean flows for one-step generative modeling** (2025), [arXiv:2505.13447](https://arxiv.org/abs/2505.13447) [cs.LG].
- [24] K. Frans, D. Hafner, S. Levine, and P. Abbeel, **One step diffusion via shortcut models** (2025), [arXiv:2410.12557](https://arxiv.org/abs/2410.12557) [cs.LG].
- [25] Y.-D. Hsieh, Y.-J. Kao, and A. W. Sandvik, Finite-size scaling method for the berezinskii-kosterlitz-thouless transition, *Journal of Statistical Mechanics: Theory and Experiment* **2013**, P09001 (2013).
- [26] Y. Tomita and Y. Okabe, Probability-changing cluster algorithm for two-dimensional XY and clock models, *Phys. Rev. B* **65**, 184405 (2002).

- [27] D. Schuh, J. Kreit, E. Berkowitz, L. Funcke, T. Luu, K. A. Nicoli, and M. Rodekamp, [Simulating the Hubbard model with equivariant normalizing flows](#) (2025), [arXiv:2501.07371 \[cond-mat.str-el\]](#).
- [28] L. Klein, A. Krämer, and F. Noe, Equivariant flow matching, in *Advances in Neural Information Processing Systems*, Vol. 36, edited by A. Oh, T. Naumann, A. Globerson, K. Saenko, M. Hardt, and S. Levine (Curran Associates, Inc., 2023) pp. 59886–59910.
- [29] W. Shi, J. Caballero, F. Huszár, J. Totz, A. P. Aitken, R. Bishop, D. Rueckert, and Z. Wang, [Real-time single image and video super-resolution using an efficient sub-pixel convolutional neural network](#) (2016), [arXiv:1609.05158 \[cs.CV\]](#).
- [30] Z. Wang and L. Wu, [Theoretical analysis of inductive biases in deep convolutional networks](#) (2024), [arXiv:2305.08404 \[cs.LG\]](#).
- [31] W. Peebles and S. Xie, [Scalable diffusion models with transformers](#) (2023), [arXiv:2212.09748 \[cs.CV\]](#).
- [32] L. Dinh, J. Sohl-Dickstein, and S. Bengio, [Density estimation using real nvp](#) (2017), [arXiv:1605.08803 \[cs.LG\]](#).
- [33] L. Dinh, D. Krueger, and Y. Bengio, [Nice: Non-linear independent components estimation](#) (2015), [arXiv:1410.8516 \[cs.LG\]](#).
- [34] G. Kanwar, M. S. Albergo, D. Boyda, K. Cranmer, D. C. Hackett, S. Racanière, D. J. Rezende, and P. E. Shanahan, Equivariant flow-based sampling for lattice gauge theory, *Phys. Rev. Lett.* **125**, 121601 (2020).
- [35] D. Boyda, G. Kanwar, S. Racanière, D. J. Rezende, M. S. Albergo, K. Cranmer, D. C. Hackett, and P. E. Shanahan, Sampling using  $SU(n)$  gauge equivariant flows, *Phys. Rev. D* **103**, 074504 (2021).
- [36] J. Shi, K. Han, Z. Wang, A. Doucet, and M. K. Titsias, [Simplified and generalized masked diffusion for discrete data](#) (2025), [arXiv:2406.04329 \[cs.LG\]](#).
- [37] I. Gat, T. Remez, N. Shaul, F. Kreuk, R. T. Q. Chen, G. Synnaeve, Y. Adi, and Y. Lipman, [Discrete flow matching](#) (2024), [arXiv:2407.15595 \[cs.LG\]](#).
- [38] P. Tuo, Z. Zeng, J. Chen, and B. Cheng, [Scalable multi-temperature free energy sampling of the alchemical space](#) (2025), [arXiv:2503.08063 \[cond-mat.stat-mech\]](#).
- [39] P. Esser, S. Kulal, A. Blattmann, R. Entezari, J. Müller, H. Saini, Y. Levi, D. Lorenz, A. Sauer, F. Boesel, D. Podell, T. Dockhorn, Z. English, K. Lacey, A. Goodwin, Y. Marek, and R. Rombach, [Scaling rectified flow transformers for high-resolution image synthesis](#) (2024), [arXiv:2403.03206 \[cs.CV\]](#).
- [40] B. F. Labs, S. Batifol, A. Blattmann, F. Boesel, S. Consul, C. Diagne, T. Dockhorn, J. English, Z. English, P. Esser, S. Kulal, K. Lacey, Y. Levi, C. Li, D. Lorenz, J. Müller, D. Podell, R. Rombach, H. Saini, A. Sauer, and L. Smith, [Flux.1 kontext: Flow matching for in-context image generation and editing in latent space](#) (2025), [arXiv:2506.15742 \[cs.GR\]](#).
- [41] I. Loshchilov and F. Hutter, [Decoupled weight decay regularization](#) (2019), [arXiv:1711.05101 \[cs.LG\]](#).
- [42] L. N. Smith and N. Topin, [Super-convergence: Very fast training of neural networks using large learning rates](#) (2018), [arXiv:1708.07120 \[cs.LG\]](#).
- [43] D. R. Nelson and J. M. Kosterlitz, Universal jump in the superfluid density of two-dimensional superfluids, *Phys. Rev. Lett.* **39**, 1201 (1977).
- [44] B. Zhang and R. Sennrich, [Root mean square layer normalization](#) (2019), [arXiv:1910.07467 \[cs.LG\]](#).
- [45] A. Vaswani, N. Shazeer, N. Parmar, J. Uszkoreit, L. Jones, A. N. Gomez, L. Kaiser, and I. Polosukhin, [Attention is all you need](#) (2023), [arXiv:1706.03762 \[cs.CL\]](#).
- [46] B. Heo, S. Park, D. Han, and S. Yun, [Rotary position embedding for vision transformer](#) (2024), [arXiv:2403.13298 \[cs.CV\]](#).
- [47] A. Paszke, S. Gross, F. Massa, A. Lerer, J. Bradbury, G. Chanan, T. Killeen, Z. Lin, N. Gimeshein, L. Antiga, A. Desmaison, A. Köpf, E. Yang, Z. DeVito, M. Raison, A. Tejani, S. Chilamkurthy, B. Steiner, L. Fang, J. Bai, and S. Chintala, [Pytorch: An imperative style, high-performance deep learning library](#) (2019), [arXiv:1912.01703 \[cs.LG\]](#).
- [48] A. Dosovitskiy, L. Beyer, A. Kolesnikov, D. Weissenborn, X. Zhai, T. Unterthiner, M. Dehghani, M. Minderer, G. Heigold, S. Gelly, J. Uszkoreit, and N. Houlsby, [An image is worth 16x16 words: Transformers for image recognition at scale](#) (2021), [arXiv:2010.11929 \[cs.CV\]](#).
- [49] M. Raghu, T. Unterthiner, S. Kornblith, C. Zhang, and A. Dosovitskiy, [Do vision transformers see like convolutional neural networks?](#) (2022), [arXiv:2108.08810 \[cs.CV\]](#).
- [50] M. Weigel, [Simulating spin models on gpu](#), *Computer Physics Communications* **182**, 1833–1836 (2011).
- [51] S. Chetlur, C. Woolley, P. Vandermersch, J. Cohen, J. Tran, B. Catanzaro, and E. Shelhamer, [cudnn: Efficient primitives for deep learning](#) (2014), [arXiv:1410.0759 \[cs.NE\]](#).